

# Protonated hydrogen cyanide as a tracer of pristine molecular gas

Y. Gong<sup>1</sup>, F. J. Du<sup>2,3</sup>, C. Henkel<sup>1,4,5</sup>, A. M. Jacob<sup>6,1</sup>, A. Belloche<sup>1</sup>, J. Z. Wang<sup>7</sup>, K. M. Menten<sup>1</sup>, W. Yang<sup>1</sup>,  
D. H. Quan<sup>8,5</sup>, C. T. Bop<sup>9</sup>, G. N. Ortiz-León<sup>10</sup>, X. D. Tang<sup>5,11,12</sup>, M. R. Rugel<sup>13,14,1</sup>, S. Liu<sup>15</sup>

<sup>1</sup> Max-Planck-Institut für Radioastronomie, Auf dem Hügel 69, D-53121 Bonn, Germany

<sup>2</sup> Purple Mountain Observatory, Chinese Academy of Sciences, Nanjing 210023, China

<sup>3</sup> School of Astronomy and Space Science, University of Science and Technology of China, Hefei 230026, China

<sup>4</sup> Astronomy Department, Faculty of Science, King Abdulaziz University, PO Box 80203, Jeddah 21589, Saudi Arabia

<sup>5</sup> Xinjiang Astronomical Observatory, Chinese Academy of Sciences, 150 Science 1-Street, Urumqi, Xinjiang 830011, China

<sup>6</sup> William H. Miller III Department of Physics & Astronomy, Johns Hopkins University, 3400 North Charles Street, Baltimore, MD 21218, USA

<sup>7</sup> Guangxi Key Laboratory for Relativistic Astrophysics, Department of Physics, Guangxi University, Nanning 530004, PR China

<sup>8</sup> Research Center for Intelligent Computing Platforms, Zhejiang Laboratory, Hangzhou 311100, China

<sup>9</sup> Univ Rennes, CNRS, IPR (Institut de Physique de Rennes) - UMR 6251, F-35000 Rennes, France

<sup>10</sup> Instituto Nacional de Astrofísica, Óptica y Electrónica, Apartado Postal 51 y 216, 72000, Puebla, Mexico

<sup>11</sup> Key Laboratory of Radio Astronomy, Chinese Academy of Sciences, Urumqi 830011, PR China

<sup>12</sup> University of Chinese Academy of Sciences, Beijing 100049, PR China

<sup>13</sup> Center for Astrophysics | Harvard & Smithsonian, 60 Garden St., Cambridge, MA 02138, USA

<sup>14</sup> National Radio Astronomy Observatory, 1003 Lopezville RD, Socorro, NM 87801, USA

<sup>15</sup> National Astronomical Observatories, Chinese Academy of Sciences, Beijing 100101, PR China

Received date ; accepted date

## ABSTRACT

**Context.** Protonated hydrogen cyanide,  $\text{HCNH}^+$ , plays a fundamental role in astrochemistry because it is an intermediary in gas-phase ion-neutral reactions within cold molecular clouds. However, the impact of the environment on the chemistry of  $\text{HCNH}^+$  remains poorly understood.

**Aims.** We aim to study  $\text{HCNH}^+$ , HCN, and HNC, as well as two other chemically related ions,  $\text{HCO}^+$  and  $\text{N}_2\text{H}^+$ , in different star formation regions in order to investigate how the environment influences the chemistry of  $\text{HCNH}^+$ .

**Methods.** With the IRAM-30 m and APEX-12 m telescopes, we carried out  $\text{HCNH}^+$ ,  $\text{H}^{13}\text{CN}$ ,  $\text{HN}^{13}\text{C}$ ,  $\text{H}^{13}\text{CO}^+$ , and  $\text{N}_2\text{H}^+$  imaging observations toward two dark clouds, the Serpens filament and Serpens South, both of which harbor sites of star formation including protostellar objects as well as regions that are quiescent.

**Results.** We report the first robust distribution of  $\text{HCNH}^+$  in the Serpens filament and in Serpens South. Our data suggest that  $\text{HCNH}^+$  is abundant in cold and quiescent regions, but is deficient in active star-forming regions. The observed  $\text{HCNH}^+$  fractional abundances relative to  $\text{H}_2$  range from  $3.1 \times 10^{-11}$  in protostellar cores to  $5.9 \times 10^{-10}$  in prestellar cores, and the  $\text{HCNH}^+$  abundance generally decreases with increasing  $\text{H}_2$  column density, which suggests that  $\text{HCNH}^+$  coevolves with cloud cores. Our observations and modeling results suggest that the abundance of  $\text{HCNH}^+$  in cold molecular clouds is strongly dependent on the  $\text{H}_2$  number density. The decrease in the abundance of  $\text{HCNH}^+$  is caused by the fact that its main precursors (e.g., HCN and HNC) undergo freeze-out as the number density of  $\text{H}_2$  increases. However, current chemical models cannot explain other observed trends, such as the fact that the abundance of  $\text{HCNH}^+$  shows an anti-correlation with that of HCN and HNC, but a positive correlation with that of  $\text{N}_2\text{H}^+$  in the southern part of the Serpens South northern clump. This indicates that additional chemical pathways have to be invoked for the formation of  $\text{HCNH}^+$  via molecules like  $\text{N}_2$  in regions in which HCN and HNC freeze out.

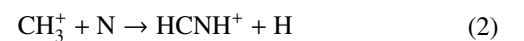
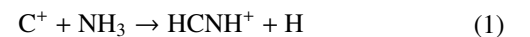
**Conclusions.** Both the fact that  $\text{HCNH}^+$  is most abundant in molecular cores prior to gravitational collapse and the fact that low- $J$   $\text{HCNH}^+$  transitions have very low  $\text{H}_2$  critical densities make this molecular ion an excellent probe of pristine molecular gas.

**Key words.** ISM: clouds — radio lines: ISM — Astrochemistry — ISM: molecules — ISM: abundances

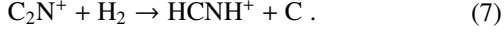
## 1. Introduction

Protonated hydrogen cyanide or iminomethylum,  $\text{HCNH}^+$ , is one of the fundamental molecular ions in the interstellar medium (ISM). Ions play an important role in interstellar chemistry as essential intermediaries in the ion-neutral reactions that dominate gas-phase chemistry in cold molecular clouds (e.g., [Agúndez & Wakelam 2013](#), and references therein). The chemistry of  $\text{HCNH}^+$  in dense and cold regions has been extensively investigated. This ion is mainly produced by ion-neutral reactions

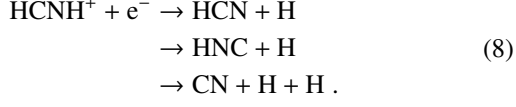
([Turner et al. 1990](#); [Schilke et al. 1991](#); [Herbst et al. 2000](#); [Loison et al. 2014a](#); [Quénard et al. 2017](#); [Fontani et al. 2021](#)), for instance:



Send *offprint requests* to: Y. Gong, e-mail: [ygong@mpi-fr-bonn.mpg.de](mailto:ygong@mpi-fr-bonn.mpg.de)



On the other hand,  $\text{HCNH}^+$  is thought to be mainly destroyed by dissociative recombination reactions:



Reactions (8) are exothermic, which suggests that  $\text{HCNH}^+$  is the main precursor of CN, HCN, and HNC (Herbst & Klemperer 1973; Herbst 1978). The chemical pathway of forming CN is energetically unfavorable in cold molecular clouds, because the simultaneous dissociation of the C-H and N-H bonds requires two electron excitations (e.g., Shiba et al. 1998). Theoretical and observational studies support the notions that reactions (8) are the main pathways to produce HCN and HNC (e.g., Shiba et al. 1998; Hirota et al. 1998; Aalto et al. 2002), and that the branching ratios to produce HCN and HNC are nearly identical at low temperatures (e.g., Mendes et al. 2012; Loison et al. 2014a; Fontani et al. 2021).

$\text{HCNH}^+$  is a simple linear molecule with a small dipole moment of 0.29 D (Botschwina 1986). It was first discovered in Sgr B2 via the detection of its three lowest rotational transitions (Ziurys & Turner 1986), and was subsequently observed in many other dense molecular clouds (e.g., Schilke et al. 1991; Ziurys et al. 1992; Hezareh et al. 2008; Quénard et al. 2017; Fontani et al. 2021). This suggests that  $\text{HCNH}^+$  is ubiquitous in molecular clouds.

Due to the nonzero nuclear spin of nitrogen,  $\text{HCNH}^+$  transitions show electric quadrupole hyperfine structure (HFS) splitting. Spectra in which the HFS of the  $\text{HCNH}^+ J = 1-0$  transition is resolved were presented, for example, by Ziurys et al. (1992) for TMC1<sup>1</sup> and by Quénard et al. (2017) for L1544, which are both chemically well-studied dark clouds. Fontani et al. (2021) performed a survey of  $\text{HCNH}^+ (3-2)$  toward 26 high-mass star-forming cores, and reported the detection of this molecule in 16 targets. This study and the ones mentioned above suggest that the typical fractional abundance of  $\text{HCNH}^+$  with respect to  $\text{H}_2$  spans a range of two orders of magnitude, from  $10^{-11}$  to  $3 \times 10^{-9}$ . Quénard et al. (2017) found that the observed  $\text{HCNH}^+$  and  $\text{HC}_3\text{NH}^+$  abundances in the dark cloud L1544 could not be well reproduced at the same time by astrochemical models, indicating that the chemistry related to  $\text{HCNH}^+$  is still not fully understood. Numerical simulations suggest that observations of the chemically co-evolving pair, HCN and  $\text{HCNH}^+$ , could be used to measure the ion-neutral drift velocity caused by ambipolar diffusion (Tritsis et al. 2023), which plays an important role in star formation (e.g., Mouschovias & Ciolek 1999).

Measurements using the Cassini space probe indicate that  $\text{HCNH}^+$  may also be the most abundant ion in the atmosphere of the largest satellite of Saturn, Titan (Cravens et al. 2006). This molecular ion was not detected in Comet Hale-Bopp (also known as C/1995 O1; Ziurys et al. 1999). These authors reported an upper limit of  $1.9 \times 10^{13} \text{ cm}^{-2}$  for its column density and an

<sup>1</sup> TMC1 harbors two chemically different dense cores which are known as the cyanopolyne peak and the ammonia peak (e.g., Toelle et al. 1981; Pratap et al. 1997). Throughout this paper, when we refer to TMC1, we mean to the cyanopolyne peak, toward which the spectrum shown by Ziurys et al. (1992) was taken, rather than the ammonia peak.

abundance ratio  $[\text{HCN}]/[\text{HCNH}^+]$  of  $\geq 1$  in this comet. Given all this, a thorough understanding of the chemistry of  $\text{HCNH}^+$  in molecular clouds is still elusive, but is essential for us to gain insights into the process of chemical evolution of the ISM and star formation.

Observations have shown that the environment of star-forming regions can strongly affect their chemistry (e.g., Jørgensen et al. 2020). However, the influence of the environment on the  $\text{HCNH}^+$  fractional abundance is still unknown. From an observational perspective, single-pointing studies of dense cores can result in loose constraints, whereas mapping studies can better address this issue. So far,  $\text{HCNH}^+$  has rarely been mapped. Because  $\text{HCNH}^+ (3-2)$  is blended with an unidentified line at 222325 MHz (possibly from  $\text{CH}_3\text{OCH}_3$ ) in the study of Sgr B2 in Schilke et al. (1991) due to the broad line widths, the map of the blended line can hardly be used to reliably trace the distribution of  $\text{HCNH}^+$  in this cloud. Therefore, the spatial distribution of  $\text{HCNH}^+$  in molecular clouds remains largely unexplored.

At a distance of  $\sim 440$  pc (Dzib et al. 2010; Ortiz-León et al. 2017, 2018; Zucker et al. 2019; Ortiz-León et al. 2023), Serpens South and the Serpens filament are known as two of the nearest infrared dark clouds (IRCDs). Both only harbor low-mass young stellar objects (YSOs; e.g., Gutermuth et al. 2008; Gong et al. 2018) and both contain parts that are quiescent as well as parts with active star formation (e.g., Friesen et al. 2013; Gong et al. 2021), which allows us to probe the influence of star formation on the chemistry.

Serpens South contains one of the nearest and youngest stellar protoclusters, the Serpens South cluster (SSC), while its northern clump (labeled as SSN hereafter) is quiescent. There are powerful outflows arising in SSC (e.g., Nakamura et al. 2011, 2014; Plunkett et al. 2015a,b; Zhang et al. 2015; Mottram et al. 2017), at the base of one of which  $\text{H}_2\text{O}$  masers are located (Ortiz-León et al. 2021). In contrast, SSN is found to have high abundances of carbon-chain molecules (Friesen et al. 2013, 2016; Li et al. 2016); recently even benzonitrile,  $c\text{-C}_6\text{H}_5\text{CN}$ , has been detected (Burkhardt et al. 2021).

A similar trend is also observed in the Serpens filament that is quiescent in the southeast and shows signs of star formation in the northwest (Gong et al. 2018, 2021). Star formation in Serpens South is much more active than in the Serpens filament, which allows us to probe different levels of star formation feedback on the chemistry. Furthermore, the two regions have typical line widths of  $\lesssim 2 \text{ km s}^{-1}$  (e.g., Levshakov et al. 2013, 2014; Friesen et al. 2016; Gong et al. 2021), which reduces the level of line confusion, which can be a significant problem for observations of the  $\text{HCNH}^+ (3-2)$  transition in regions like Sgr B2 (Schilke et al. 1991). Therefore, the Serpens filament and Serpens South are ideal sites to study the influence of the environment on the  $\text{HCNH}^+$  fractional abundance. In this work, we present a mapping study of  $\text{HCNH}^+$  to unveil its distribution and characterize its chemistry in these two regions.

Our observations are described in Sect. 2. In Sect. 3, we report our results, which are discussed in Sect. 4. Lastly, our summary and conclusions are presented in Sect. 5.

## 2. Observations and data reduction

### 2.1. IRAM-30 m and APEX-12 m observations

We carried out  $\text{HCNH}^+ (1-0)$ ,  $\text{HCNH}^+ (2-1)$ ,  $\text{H}^{13}\text{CN} (1-0)$ ,  $\text{HN}^{13}\text{C} (1-0)$ ,  $\text{H}^{13}\text{CO}^+ (1-0)$ , and  $\text{N}_2\text{H}^+ (1-0)$  imaging observations toward Serpens South and the Serpens filament with

the IRAM-30m telescope<sup>2</sup> during 2019 September 27–29, 2020 December 26–27, 2021 August 21–24, and October 22–25. During the observations, the EMIR dual-sideband and dual-polarization receivers (E090 and E150) were used as frontend (Carter et al. 2012), while Fast Fourier Transform Spectrometers (FFTSs) were used as backend. For the HCNH<sup>+</sup> (1–0) and HCNH<sup>+</sup> (2–1) lines, we used the narrow FFTSs, which provided a channel width of 50 kHz, corresponding to a velocity spacing of 0.2 km s<sup>-1</sup> at 74 GHz and 0.1 km s<sup>-1</sup> at 148 GHz (see also Table 1). For H<sup>13</sup>CN (1–0), HN<sup>13</sup>C (1–0), H<sup>13</sup>CO<sup>+</sup> (1–0), and N<sub>2</sub>H<sup>+</sup> (1–0), FFTSs with a channel width of 50 kHz and 250 kHz are used for the Serpens filament and Serpens South, respectively. The corresponding channel spacings in units of km s<sup>-1</sup> are given in Table 1.

Using the Atacama Pathfinder EXperiment 12 meter sub-millimeter telescope (APEX<sup>3</sup>; Güsten et al. 2006), we carried out HCNH<sup>+</sup> (3–2) mapping observations toward the Serpens filament during 2019 April 29 – May 1 (project code: M9511A\_103) and pointed HCNH<sup>+</sup> (3–2) observations toward Serpens South during 2018 May 25 – 2018 July 13 (project code: M9506A\_101). The coordinates of the pointed positions are given in Table 2. A PI230 sideband separated and dual-polarization receiver<sup>4</sup>, built by the Max Planck Institute for Radio Astronomy, was employed as frontend, while FFTSs were adopted as backend (Klein et al. 2012). Each FFTS encompasses a bandwidth of 4 GHz and 65536 channels, resulting in a channel width of 61 kHz. The corresponding velocity spacing is 0.08 km s<sup>-1</sup> for HCNH<sup>+</sup> (3–2) (see also Table 1). The observations were performed in the position-switching or On-The-Fly mode using the APECS software (Muders et al. 2006).

At the beginning of each observing session, pointing and focus were investigated toward bright continuum sources like Mars and Mercury. Pointing was regularly checked on nearby bright sources every hour, and its accuracy was found to be within 5". A single on-off observation toward SSC was performed to verify each frequency setup before mapping. The regions were observed in two orthogonal directions using the On-The-Fly mode. The standard chopper wheel method was used for calibrations and correcting the atmospheric attenuation of the IRAM-30 m observations (Ulich & Haas 1976), while an extension of the method using three loads was applied to the APEX-12 m observations. The calibration was undertaken about every 10 minutes. The antenna temperature,  $T_A^*$ , was converted to main beam temperature,  $T_{mb}$ , by applying the relation,  $T_{mb} = T_A^* \eta_f / \eta_{mb}$ , where  $\eta_f$  and  $\eta_{mb}$  are the forward efficiency and main beam efficiency<sup>5</sup>, respectively (see Table 1 for the values). The uncertainties in the absolute flux calibration are assumed to be 10% in this work. The observed spectral lines, their rest frequencies, and other spectroscopic and observational information are listed in Table 1. Velocities with respect to the local standard of rest (LSR) are reported throughout this work.

The GILDAS<sup>6</sup> software was used to reduce the spectral line data (Pety 2005), and a first-order baseline was subtracted from each spectrum. For all the maps, raw spectra were gridded into a data cube with a pixel size of 5"×5". Since the HCNH<sup>+</sup> emission in our sources is generally weak and has a smooth extent, all spectral data are smoothed to a half power beam width (HPBW) of 36"×3. This facilitates the comparison with the *Herschel* H<sub>2</sub> column density and dust temperature maps (see Sect. 2.2).

## 2.2. Archival data

Dust-based H<sub>2</sub> column density and dust temperature maps<sup>8</sup> were derived from spectral energy distributions (SEDs) fitted to *Herschel* data at four far-infrared bands, that is, 160, 250, 350, and 500 μm (André et al. 2010; Könyves et al. 2015; Fiorellino et al. 2021). These maps also have an angular resolution of 36"×3.

NH<sub>3</sub> and CO archival data are only available for Serpens South. For NH<sub>3</sub> in Serpens South, we utilized the data products<sup>9</sup> from observations with the Green Bank Telescope (Friesen et al. 2016). The corresponding HPBW is 32". CO (3–2) data<sup>10</sup> of Serpens South were obtained with the Atacama Submillimeter Telescope Experiment (ASTE) 10 m telescope. The data that we retrieved has a HPBW of 22" and a channel width of ~0.11 km s<sup>-1</sup>. The typical noise level is 0.11 K on a  $T_A^*$  scale at a velocity spacing of 0.5 km s<sup>-1</sup>. The main beam efficiency is 0.57 at 345 GHz. Details of the observations are presented in Nakamura et al. (2011).

## 3. Results

### 3.1. Molecular distribution

Figure 1 presents the distributions of HCNH<sup>+</sup> (2–1) and HCNH<sup>+</sup> (3–2) emission toward the Serpens filament. The overall distributions of the two transitions are similar in the Serpens filament, with slight differences arising from the fact that the signal-to-noise ratio of HCNH<sup>+</sup> (3–2) is lower than that of HCNH<sup>+</sup> (2–1). HCNH<sup>+</sup> is detected toward three dense cores, called bolo2, bolo4, and bolo12 by Enoch et al. (2007). The name “bolo” refers to Bolocam that is a large-format bolometric camera of the Caltech Submillimeter Observatory (Glenn et al. 2003). The emission is the brightest in bolo4 followed by bolo12. Based on the comparison with the *Herschel* results, we find that the detected HCNH<sup>+</sup> emission arises from regions with dust temperatures,  $T_d$ , of  $\lesssim 12$  K and H<sub>2</sub> column densities  $> 1 \times 10^{22}$  cm<sup>-2</sup> (Fiorellino et al. 2021), which indicates that the observed HCNH<sup>+</sup> emission mainly arises from cold and high H<sub>2</sub> column density regions. Toward the YSO emb10<sup>11</sup>, which drives a molecular outflow (Gong et al. 2021, 2023, see also Fig. 1c and 1d for the outflow lobes), the HCNH<sup>+</sup> emission appears to be absent.

Figure 2 presents the distribution of HCNH<sup>+</sup> (2–1) emission toward Serpens South with the purple crosses marking the positions of the prestellar dense cores extracted from the *Herschel*

<sup>2</sup> This work is based on observations carried out under project numbers 023-19, 127-20, 028-21 with the IRAM-30 m telescope. IRAM is supported by INSU/CNRS (France), MPG (Germany) and IGN (Spain).

<sup>3</sup> This publication is based on data acquired with the Atacama Pathfinder Experiment (APEX). APEX is a collaboration between the Max-Planck-Institut für Radioastronomie, the European Southern Observatory, and the Onsala Space Observatory.

<sup>4</sup> <https://www.eso.org/public/teles-instr/apex/pi230/>

<sup>5</sup> see <https://publicwiki.iram.es/Iram30mEfficiencies> and <http://www.apex-telescope.org/telescope/efficiency/>

<sup>6</sup> <https://www.iram.fr/IRAMFR/GILDAS/>

<sup>8</sup> [http://www.herschel.fr/cea/gouldbelt/en/Phoceia/Vie\\_des\\_labos/Ast/ast\\_visu.php?id\\_ast=66](http://www.herschel.fr/cea/gouldbelt/en/Phoceia/Vie_des_labos/Ast/ast_visu.php?id_ast=66)

<sup>9</sup> <https://dataverse.harvard.edu/dataset.xhtml?persistentId=doi:10.7910/DVN/SDHQRP>

<sup>10</sup> <http://th.nao.ac.jp/MEMBER/nakamrfm/sflegacy/data.html>

<sup>11</sup> The term “emb” is the abbreviation of “embedded” (Enoch et al. 2009).

**Table 1.** Observational and spectroscopic parameters related to the molecular lines presented in this work.

Transition (1)	Frequency (MHz) (2)	$E_u/k$ (K) (3)	$A$ ( $s^{-1}$ ) (4)	$\mu$ (D) (5)	$n_c(\text{H}_2)$ ( $\text{cm}^{-3}$ ) (6)	$\theta_{\text{beam}}$ ( $''$ ) (7)	$\eta_{\text{mb}}/\eta_{\text{f}}$ (8)	Serpens filament		Serpens South		Telescope (13)
								$\sigma$ (mK) (9)	$\delta v$ ( $\text{km s}^{-1}$ ) (10)	$\sigma$ (mK) (11)	$\delta v$ ( $\text{km s}^{-1}$ ) (12)	
$\text{HCNH}^+ J = 1 - 0$	74111.302(3)	3.6	$1.4 \times 10^{-7}$	0.29	$2.0 \times 10^2$	33	0.87	–	–	51	0.20	IRAM-30 m
$\text{HCNH}^+ J = 2 - 1$	148221.450(17)	10.7	$1.3 \times 10^{-6}$	0.29	$1.7 \times 10^3$	18	0.78	21	0.21	58	0.21	IRAM-30 m
$\text{HCNH}^+ J = 3 - 2$	222329.277(8)	21.3	$4.9 \times 10^{-6}$	0.29	$5.2 \times 10^3$	27	0.80	28	0.08	20	0.08	APEX
$\text{H}^{13}\text{CN } J = 1 - 0$	86339.921(1)	4.1	$2.2 \times 10^{-5}$	2.99	$5.3 \times 10^5$	28	0.85	22	0.17	24	0.68	IRAM-30 m
$\text{HN}^{13}\text{C } J = 1 - 0$	87090.825(4)	4.2	$1.9 \times 10^{-5}$	2.70	$1.4 \times 10^5$	28	0.85	18	0.17	26	0.67	IRAM-30 m
$\text{H}^{13}\text{CO}^+ J = 1 - 0$	86754.288(5)	4.2	$3.9 \times 10^{-5}$	3.90	$6.2 \times 10^4$	28	0.85	40	0.17	27	0.68	IRAM-30 m
$\text{N}_2\text{H}^+ J = 1 - 0$	93173.398(1)	4.5	$3.6 \times 10^{-5}$	3.40	$6.1 \times 10^4$	26	0.84	19	0.16	26	0.63	IRAM-30 m

**Notes.** (1) Observed transition. All transitions were observed in the On-The-Fly mode, except for  $\text{HCNH}^+$  (3–2) which was observed as single pointing toward Serpens South. (2) Rest frequency taken from the Cologne Database for Molecular Spectroscopy (CDMS<sup>7</sup>, [Endres et al. 2016](#)). Uncertainties in the last digits are given in parentheses. For the observed lines, only the frequency of the strongest HFS component is listed. (3) Upper energy level of the observed transition. (4) Einstein A coefficient. (5) Dipole moment from CDMS ([Endres et al. 2016](#)). (6) Optically thin  $\text{H}_2$  critical density at a kinetic temperature of 10 K. The critical densities of  $\text{HCNH}^+$  transitions are calculated using the collisional rate coefficients from [Bop & Lique \(2023\)](#) and Eq. (4) in [Shirley \(2015\)](#). For the other lines, the values are directly taken from Table 1 in [Shirley \(2015\)](#). The critical density of  $\text{HN}^{13}\text{C}$  (1–0) is assumed to be the same as that of HNC (1–0). (7) HPBW. (8)  $\eta_{\text{f}}$  and  $\eta_{\text{mb}}$  are the forward efficiency and main beam efficiency, respectively. (9) RMS level at the smoothed angular resolution of  $36''.3$ . (10) Velocity channel spacing. (11) RMS level at the smoothed angular resolution of  $36''.3$ . For pointed  $\text{HCNH}^+$  (3–2) observations in Serpens South, the RMS level is estimated at the original angular resolution of  $27''$ . (12) Velocity channel spacing. (13) Telescope.

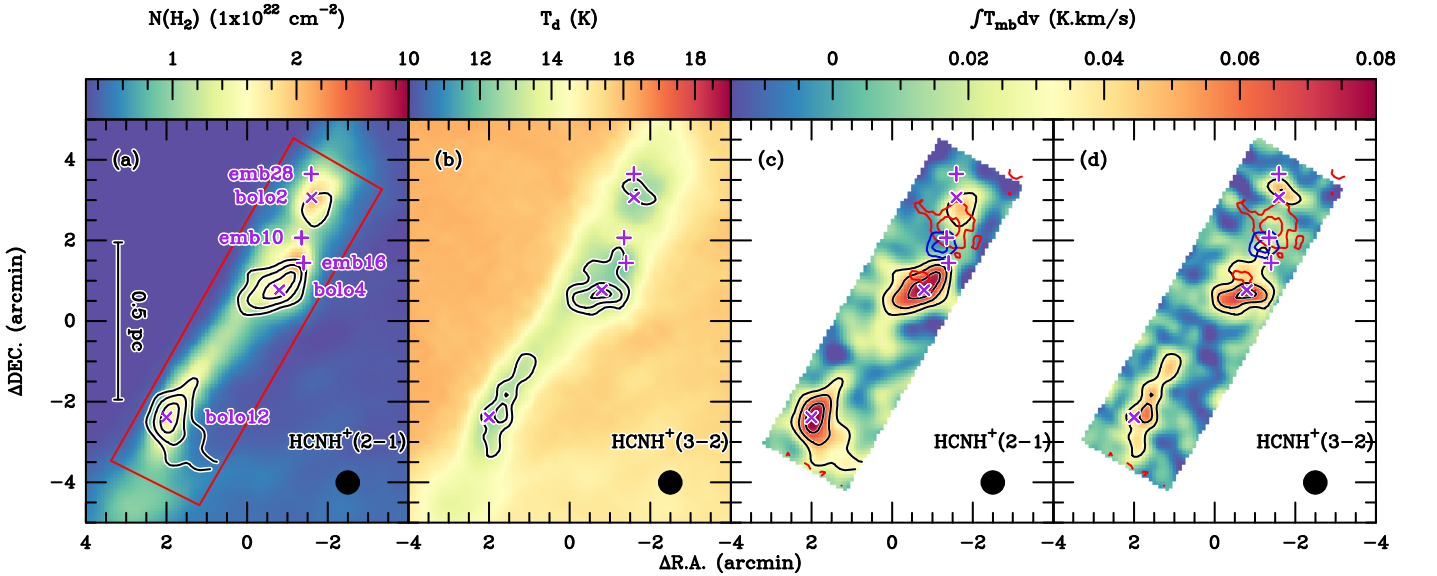


**Fig. 1.** (a) *Herschel*  $\text{H}_2$  column density map of the Serpens filament ([Fiorellino et al. 2021](#)) overlaid with the  $\text{HCNH}^+$  (2–1) integrated intensity contours. The velocity range over which the  $\text{HCNH}^+$  (2–1) intensity map is integrated is  $7.7\text{--}8.7 \text{ km s}^{-1}$ . The contours start at  $0.03 \text{ K km s}^{-1}$  ( $3\sigma$ ) and increase by  $0.02 \text{ K km s}^{-1}$ . The red boundary represents the region mapped by our IRAM 30-m and APEX 12-m observations. (b) *Herschel* dust temperature map ([Fiorellino et al. 2021](#)) overlaid with the  $\text{HCNH}^+$  (3–2) integrated intensity contours. The velocity range over which the  $\text{HCNH}^+$  (3–2) intensity is integrated is  $7.7\text{--}8.7 \text{ km s}^{-1}$ . The contours start at  $0.03 \text{ K km s}^{-1}$  ( $3\sigma$ ) and increase by  $0.02 \text{ K km s}^{-1}$ . (c)  $\text{HCNH}^+$  (2–1) integrated intensity map overlaid with the blue-, and red-shifted outflow lobes of  $^{13}\text{CO}$  (2–1) that are driven by emb10 ([Gong et al. 2021](#)). The black contours are the same as in panel a. (d) Similar to panel c, but for  $\text{HCNH}^+$  (3–2). The beam size is shown in the lower right corner of each panel. In all panels, the (0, 0) offset corresponds to  $\alpha_{\text{J2000}}=18^{\text{h}}28^{\text{m}}50^{\text{s}}.4$ ,  $\delta_{\text{J2000}}=00^{\circ}49'58''.72$ . The three purple plus signs indicate the positions of the three embedded YSOs, emb10, emb16, and emb 28 ([Enoch et al. 2009](#)), while the three purple crosses mark the positions of three 1.1 mm dust continuum cores, bolo2, bolo4, and bolo12 ([Enoch et al. 2007](#)).

dust continuum maps ([Könyves et al. 2015](#)). We find that the  $\text{HCNH}^+$  emission is prominent toward SSN, but barely detected toward SSC. The brightest  $\text{HCNH}^+$  emission lies in the southern part of SSN (labeled as SSN1 in Fig. 2b), which is slightly offset from the dust continuum peak (the prestellar core KAM280, No. 280 in [Könyves et al. 2015](#), also named as SerS MM9 by [Maury et al. 2011](#)). The emission in the northern part of SSN (labeled as SSN2 in Fig. 2b) and the weak emission in SSC appear

not to be associated with any dust continuum core. The detected  $\text{HCNH}^+$  emission in SSN comes from regions with  $T_{\text{d}} \leq 12 \text{ K}$ , similar to those in the Serpens filament. We also note that the weak  $\text{HCNH}^+$  emission in SSC arises from a slightly warmer region with  $T_{\text{d}} \sim 15 \text{ K}$ . The ammonia observations ([Friesen et al. 2016](#)) confirm that the gas kinetic temperatures are  $\leq 12 \text{ K}$  in SSN and  $\sim 15 \text{ K}$  in SSC. On the other hand, the  $\text{HCNH}^+$  emitting region in Serpens South has  $\text{H}_2$  column densities  $\geq 4 \times 10^{22} \text{ cm}^{-2}$ .

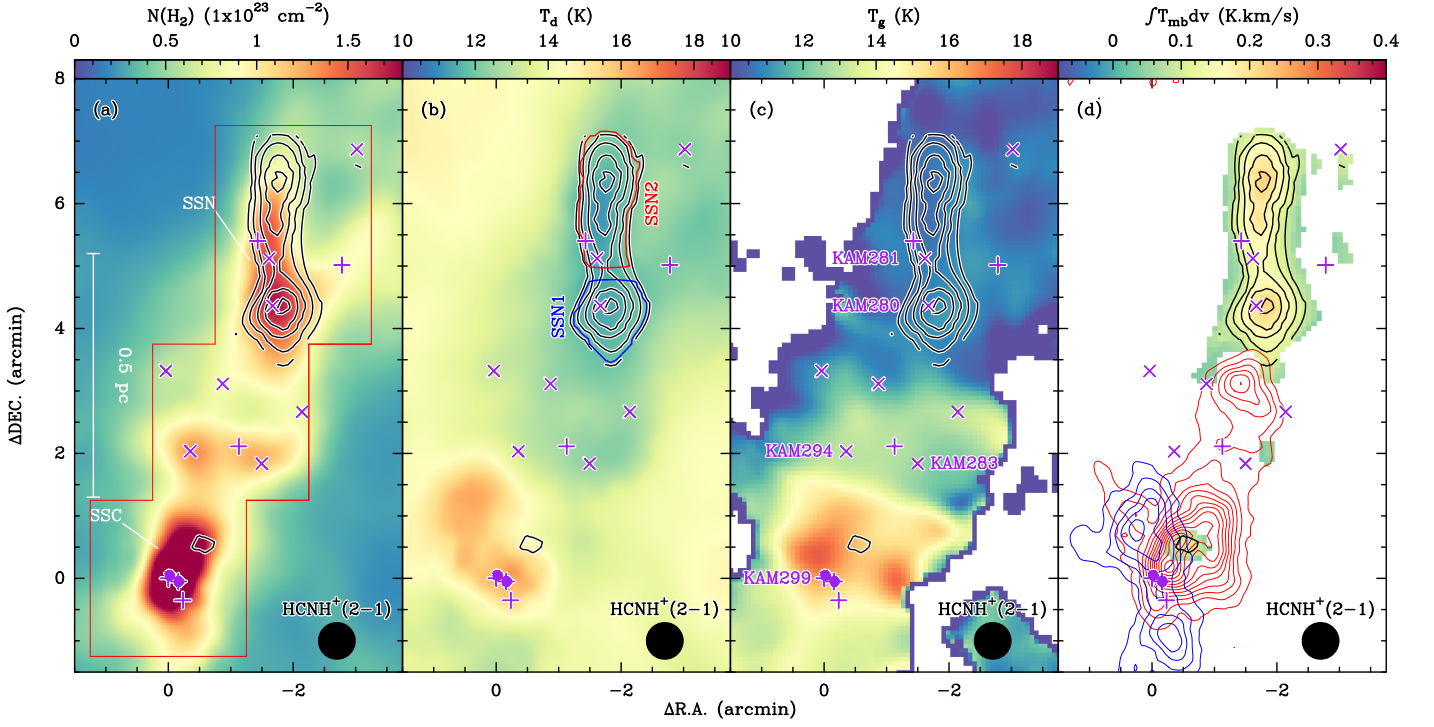


**Fig. 2.** (a) *Herschel*  $H_2$  column density map of Serpens South (Könyves et al. 2015) overlaid with  $HCNH^+$  (2–1) integrated intensity contours. The velocity range over which the  $HCNH^+$  (2–1) intensity is integrated is  $6.5\text{--}8.5 \text{ km s}^{-1}$ . The contours start at  $0.09 \text{ K km s}^{-1}$  ( $3\sigma$ ) and increase by  $0.03 \text{ K km s}^{-1}$ . The red boundary represents the region mapped by our IRAM-30 m observations. (b) *Herschel* dust temperature map (Könyves et al. 2015) overlaid with the  $HCNH^+$  (2–1) integrated intensity contours that are the same as in panel a. SSN is further divided into two subregions, SSN1 and SSN2, which are labeled in this panel. (c) Gas kinetic temperature map derived from ammonia observations (Friesen et al. 2016) overlaid with the  $HCNH^+$  (2–1) integrated intensity contours that are the same as in panel a. (d)  $HCNH^+$  (2–1) integrated intensity map overlaid with the CO (3–2) blueshifted and redshifted outflow lobes from the SSC (Nakamura et al. 2011). The black contours represent  $HCNH^+$  (2–1) integrated intensity as the contours in panel a. The beam size is shown in the lower right corner of each panel. In all panels, the (0, 0) offset corresponds to  $\alpha_{J2000}=18^h30^m04^s19$ ,  $\delta_{J2000}=-02^{\circ}03'05''.5$ . The two purple circles represent the two 22 GHz water masers (Ortiz-León et al. 2021). The purple pluses indicate the positions of deeply embedded YSOs (Könyves et al. 2015; Sun et al. 2022), while the purple crosses mark the positions of the prestellar dense cores extracted from the *Herschel* dust continuum maps (Könyves et al. 2015).

In Fig. 2d, the weak  $HCNH^+$  emission in SSC appears to coincide with the peak of the redshifted outflow lobe (Nakamura et al. 2011) that is about  $30''$  offset from the  $H_2$  column density peak. However, the observed line width of the weak emission is as narrow as  $0.45 \pm 0.21 \text{ km s}^{-1}$ , which does not suggest that the weak  $HCNH^+$  emission is produced by the outflow shocks.

As shown in Fig. 3, our APEX-12 m pointed observations toward Serpens South have led to the detection of  $HCNH^+$  (3–2) in seven dense cores with  $T_d \lesssim 18 \text{ K}$ . The brightest  $HCNH^+$  (3–2) emission comes from KAM280, which is in agreement with our  $HCNH^+$  (2–1) map. The detection of  $HCNH^+$  (3–2) in KAM299 (also known as SerS-MM18) suggests that  $HCNH^+$  exists in SSC, but that its emission is much weaker than in SSN. The observed line profiles are commonly Gaussian-like. In order to derive the observational parameters, we employ a single-Gaussian component to fit the observed spectra, because the HFS lines of the 3–2 transition are too close in frequency to be separated. The fitted peak main beam brightness temperature, velocity centroids, and full width at half maximum (FWHM) line widths are given in Table 2.

We also mapped Serpens South in  $HCNH^+$  (1–0) but no emission was detected. This places a  $3\sigma$  upper limit of  $0.15 \text{ K}$  for the peak intensity. In order to detect the weak  $HCNH^+$  (1–0) emission, we average all the  $HCNH^+$  (1–0) spectra in the region where the  $HCNH^+$  (2–1) integrated intensities are higher than

$3\sigma$ . The results are shown in Fig. 4. The  $HCNH^+$  (1–0) average spectrum has a  $\sim 5\sigma$  detection and peaks at exactly the same velocity as its  $HCNH^+$  (2–1) counterpart, securing the detection of  $HCNH^+$  (1–0). However, the contributions of the HFS satellite lines are not discernible in Fig. 4 at the current noise level. The detected lines are mainly attributed to the contributions of the  $F = 2 - 1$  and  $F = 3 - 2$  hyperfine lines for  $J = 1 - 0$  and  $J = 2 - 1$ , respectively.

In this work, we use  $H^{13}CN$  (1–0),  $HN^{13}C$  (1–0),  $H^{13}CO^+$  (1–0), and  $N_2H^+$  (1–0) emission as proxies to investigate the distributions of HCN, HNC,  $HCO^+$ , and  $N_2H^+$  emission toward the Serpens filament and Serpens South. The Serpens filament has been mapped in  $N_2H^+$  (1–0) by Gong et al. (2018). Serpens South has been mapped in  $N_2H^+$  (1–0) and  $H^{13}CO^+$  (1–0) by Kirk et al. (2013) and Tanaka et al. (2013). In comparison to these studies, the observations presented here provide either higher angular resolutions or better sensitivities or both. Figures 5–6 present the integrated intensity maps of  $HCNH^+$ ,  $H^{13}CN$ ,  $HN^{13}C$ ,  $H^{13}CO^+$ , and  $N_2H^+$ . Comparing the distribution of  $HCNH^+$  with those of the other tracers in the Serpens filament (see Fig. 5), we find that the different tracers have nearly the same distribution toward bolo12, which is not affected by star formation. Toward bolo4, the distribution of  $HCNH^+$  is similar to those of  $H^{13}CN$  and  $HN^{13}C$ , but is slightly different from those of  $H^{13}CO^+$  and  $N_2H^+$  (i.e., the peaks of the

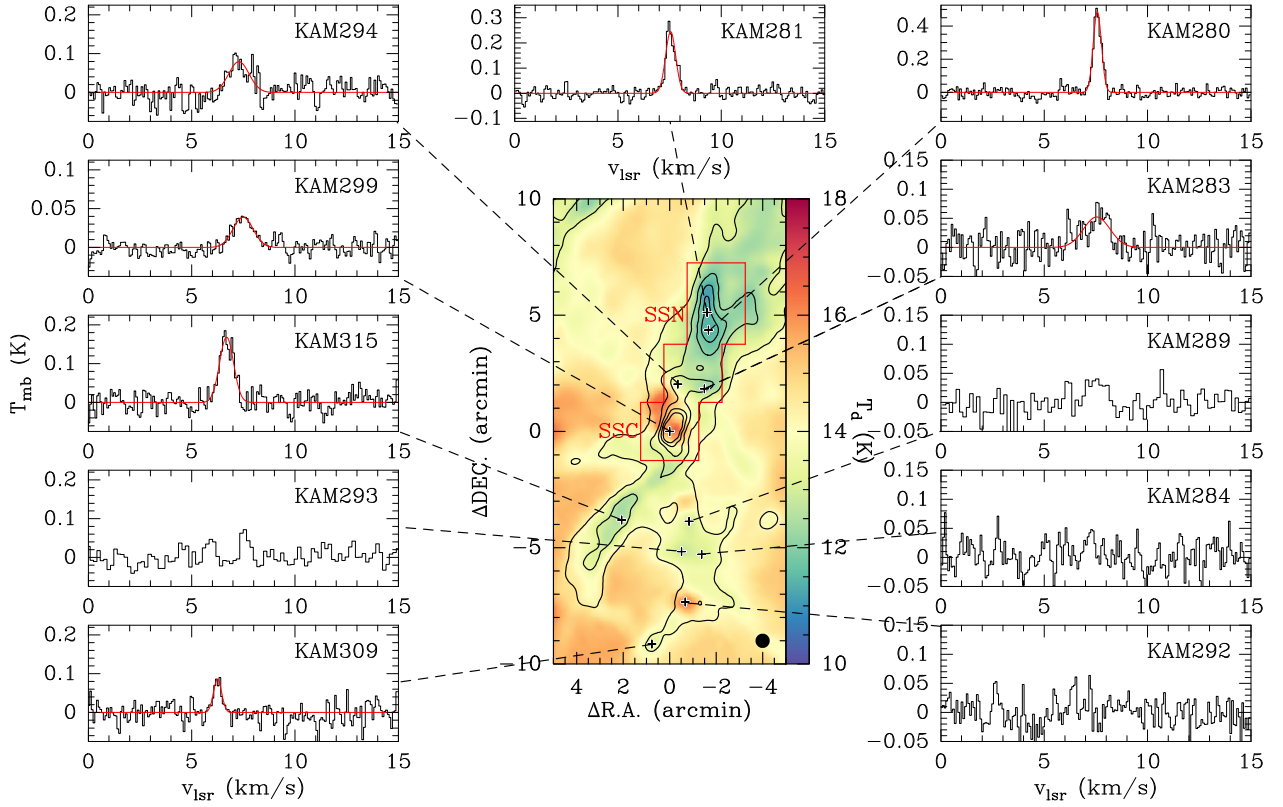


**Fig. 3.** *Herschel* dust temperature map of Serpens South (Könyves et al. 2015) overlaid with  $\text{H}_2$  column density contours that start at  $2 \times 10^{22} \text{ cm}^{-2}$  and increase by  $2 \times 10^{22} \text{ cm}^{-2}$ . The beam size is shown in the lower right corner of the central panel. The (0, 0) offset corresponds to  $\alpha_{\text{J2000}} = 18^{\text{h}}30^{\text{m}}04^{\text{s}}.19$ ,  $\delta_{\text{J2000}} = -02^{\circ}03'05''.5$ . The region mapped in  $\text{HCNH}^+$  (2–1) is indicated by the red boundary. The positions toward which pointed observations of  $\text{HCNH}^+$  (3–2) were carried out are indicated by the black plus signs in Serpens South. To the spectra: observed  $\text{HCNH}^+$  (3–2) spectra are displayed in black, while Gaussian fits to the line profiles are shown in red. The source name is indicated in the upper right corner of each panel.

**Table 2.** Spectral line properties of the  $\text{HCNH}^+$  (3–2) transition observed toward the selected positions in Serpens South.

Name	$\alpha_{\text{J2000}}$ (h m s)	$\delta_{\text{J2000}}$ ( $^{\circ}$ ' ")	$T_{\text{p}}$ (mK)	$v_{\text{lsr}}$ ( $\text{km s}^{-1}$ )	$\Delta v$ ( $\text{km s}^{-1}$ )	Class	Other names
(1)	(2)	(3)	(4)	(5)	(6)	(7)	(8)
KAM280	18:29:57.50	-01:58:43.7	$485 \pm 33$	$7.57 \pm 0.01$	$0.47 \pm 0.02$	prestellar	SerS-MM9
KAM281	18:29:57.72	-01:57:58.2	$245 \pm 30$	$7.55 \pm 0.01$	$0.58 \pm 0.03$	prestellar	SerpS-MM8
KAM283	18:29:58.20	-02:01:15.2	$52 \pm 18$	$7.55 \pm 0.01$	$1.49 \pm 0.34$	prestellar	
KAM284	18:29:58.66	-02:08:22.5	<67	–	–	prestellar	
KAM289	18:30:00.85	-02:06:57.3	<56	–	–	protostellar	SerpS-MM11
KAM292	18:30:01.50	-02:10:25.5	<56	–	–	protostellar	SerpS-MM13, IRAS 18274-0212
KAM293	18:30:02.13	-02:08:15.1	<55	–	–	prestellar	SerS-MM14
KAM294	18:30:02.77	-02:01:03.4	$79 \pm 25$	$7.28 \pm 0.06$	$1.15 \pm 0.12$	prestellar	SerS-MM15
KAM299	18:30:04.19	-02:03:05.5	$39 \pm 5$	$7.49 \pm 0.05$	$1.16 \pm 0.11$	protostellar	SERS 02, SerpS-MM18
KAM309	18:30:07.24	-02:12:13.6	$84 \pm 10$	$6.25 \pm 0.04$	$0.44 \pm 0.09$	prestellar	
KAM315	18:30:12.44	-02:06:53.6	$169 \pm 21$	$6.69 \pm 0.02$	$0.80 \pm 0.05$	protostellar	SerpS-MM22

**Notes.** (1) Source name from Könyves et al. (2015). (2) Right ascension. (3) Declination. (4) Peak main beam brightness temperature. (5) Velocity centroid. (6) FWHM line width. (7) Classification from Könyves et al. (2015). (8) Other names from Maury et al. (2011) and Mottram et al. (2017).

$\text{H}^{13}\text{CO}^+$  and  $\text{N}_2\text{H}^+$  emission lie to the west of the  $\text{HCNH}^+$  emission peak). Since bolo4 lies close to the blueshifted outflow lobe from emb10 (see Fig. 1), the difference could be caused by outflow feedback.

In Serpens South (Fig. 6)  $\text{HCNH}^+$  emission is weak toward SSC, which is in stark contrast to the other four tracers which exhibit the brightest emission toward SSC. Toward SSN, the molecular morphologies are different for the various molecu-

lar gas tracers, which is more evident in Fig. 7. No molecular line emission peaks at the positions of the dust peaks. The  $\text{HCNH}^+$  emission peaks are offset from the emission peaks of other molecular line tracers, which could be (at least partially) caused by selective freeze-out processes and optical depth effects, as discussed further in Sect. 3.2.

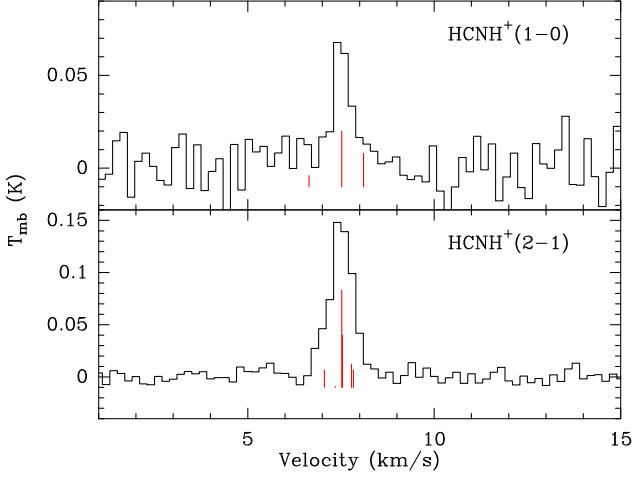


**Fig. 4.** HCNH<sup>+</sup> (1–0) and HCNH<sup>+</sup> (2–1) spectra averaged over the region where HCNH<sup>+</sup> (2–1) integrated intensities are higher than 3 $\sigma$  in Fig. 2. The positions and relative intensities of the HFS components are indicated by the red vertical lines.

### 3.2. Molecular column densities and abundances

Based on the HFS fit to the N<sub>2</sub>H<sup>+</sup> (1–0) spectra, we find that the total optical depth of N<sub>2</sub>H<sup>+</sup> (1–0) is generally larger than unity in our mapped regions. Therefore, we first apply the HFS fit to the N<sub>2</sub>H<sup>+</sup> (1–0) data cube with the PySpecKit package (Ginsburg & Mirocha 2011) to obtain the excitation temperature, total optical depth, velocity centroid, and velocity dispersion. We discard the fitted results for spectra with excitation temperatures lower than 5 $\sigma$  in order to have reliable measurements of the derived column densities. The results are shown in Figs. 8 and 9. We find that the N<sub>2</sub>H<sup>+</sup> (1–0) excitation temperatures are generally lower than 7 K in the Serpens filament, and 3.3–11.1 K in Serpens South. The highest excitation temperature of 11.1 K is found toward SSC. This is expected, because SSC tends to have the highest kinetic temperature and H<sub>2</sub> column density (see Fig. 2). The total optical depths of N<sub>2</sub>H<sup>+</sup> (1–0) become quite high toward bolo4 in the Serpens filament and SSN in Serpens South, with the highest total optical depths reaching up to  $\sim 14.5$  and  $\sim 24.5$  in bolo4 and SSN, respectively. Figures 8c and 9c present the distributions of the velocity dispersions of the N<sub>2</sub>H<sup>+</sup> emission, which further support our hypothesis that the HCNH<sup>+</sup> emission is more prominent toward the quiescent regions that have velocity dispersions  $\lesssim 0.3$  km s<sup>–1</sup>.

With the fitted values, the N<sub>2</sub>H<sup>+</sup> column densities can be estimated using Eq. (95) in Mangum & Shirley (2016),

$$N_{\text{tot}} = \frac{3h}{8\pi^3\mu^2S} \frac{Q(T_{\text{ex}})}{g_J} \exp\left(\frac{E_u}{kT_{\text{ex}}}\right) \left[\exp\left(\frac{h\nu}{kT_{\text{ex}}}\right) - 1\right]^{-1} \times \int \tau dv. \quad (9)$$

where  $h$  is the Planck constant,  $\mu$  is the dipole moment (see Table 1),  $S$  is the line strength,  $Q(T_{\text{ex}})$  is the molecular partition function at the excitation temperature,  $T_{\text{ex}}$ ,  $g_J$  describes the rotational degeneracy,  $E_u$  is the upper level energy of the transition,  $T_{\text{bg}}$  is the background temperature that is set to be 2.73 K here (Fixsen 2009), and  $\int \tau dv$  is the integrated optical depth. For linear molecules, the line strength of a transition is given as  $S = \frac{J_u}{2J_u+1}$  and the rotational degeneracy is given as  $g_J = 2J_u + 1$ , where  $J_u$  is the total angular momentum of the upper level of a given transition in a two-level system. The partition function

of linear molecules can be approximated as  $Q(T_{\text{ex}}) = \frac{kT_{\text{ex}}}{hB} + \frac{1}{3}$ , where  $B$  is the rotational constant.

With this equation, we are able to derive the column densities of N<sub>2</sub>H<sup>+</sup>. The results are shown in Figures 8d and 9d. The derived N<sub>2</sub>H<sup>+</sup> column densities are (0.4–10.8) $\times 10^{12}$  cm<sup>–2</sup> and (0.8–57.1) $\times 10^{12}$  cm<sup>–2</sup> for the Serpens filament and Serpens South, respectively. It is worth noting that the distribution of N<sub>2</sub>H<sup>+</sup> column densities is slightly different from the corresponding N<sub>2</sub>H<sup>+</sup> (1–0) integrated intensity map, which is caused by the optical depths of N<sub>2</sub>H<sup>+</sup> (1–0) and the variations of excitation temperature. Furthermore, the HCNH<sup>+</sup> emission peaks coincide with the peaks of N<sub>2</sub>H<sup>+</sup> column densities toward bolo2, bolo4, bolo12, and the peak in SSN2 in Figs. 8d and 9d, which implies that HCNH<sup>+</sup> can, similarly to N<sub>2</sub>H<sup>+</sup>, trace prestellar core centers in such regions.

Based on the HFS fit to H<sup>13</sup>CN (1–0), we find that its total optical depths can reach up to about 3. However, the HFS fitting toward the whole data cube tends to have large uncertainties for most pixels, which makes most of the fitting results unreliable. This could be caused by the anomalous line intensities of the hyperfine lines (e.g., Walmsley et al. 1982; Cernicharo et al. 1984; Loughnane et al. 2012; Jin et al. 2015; Goicoechea et al. 2022) and the relatively low signal-to-noise ratios. In order to balance the signal-to-noise ratio and optical depth effect, we use the  $F = 2 - 1$  satellite line (5/9 of the total optical depths) of H<sup>13</sup>CN (1–0) to estimate H<sup>13</sup>CN column densities in the optically thin approximation.

As for HCNH<sup>+</sup>, the peak intensities of its (2–1) and (3–2) lines are typically  $< 0.5$  K. Adopting a beam dilution factor of unity and an excitation temperature of 12 K, their peak optical depths are lower than 0.1 according to the radiative transfer equation. This suggests that HCNH<sup>+</sup> (2–1) and (3–2) are optically thin.

We performed a similar estimate for HN<sup>13</sup>C (1–0) and H<sup>13</sup>CO<sup>+</sup>(1–0). We find that these lines' peak optical depths can be higher than unity. HN<sup>13</sup>C (1–0) also has HFS components, but these components are too close in frequency to allow for an accurate determination of its optical depth. Hence, HN<sup>13</sup>C (1–0) and H<sup>13</sup>CO<sup>+</sup>(1–0) were simply assumed to be optically thin in this study. Assuming conditions of local thermodynamic equilibrium (LTE) and using the optically thin approximation, we can therefore estimate the beam-averaged column densities of these molecules. Nevertheless, we must exercise caution when interpreting the resulting H<sup>13</sup>CN, HN<sup>13</sup>C, and H<sup>13</sup>CO<sup>+</sup> column densities in regions with high peak intensities, as they can be only taken as the lower limits in case of high optical depths.

Excitation temperatures are needed to determine the molecular column densities. In the optically thin regime, the HCNH<sup>+</sup> excitation temperature can be estimated from the line ratio between HCNH<sup>+</sup> (2–1) and (3–2). Because of the relatively low signal-to-noise ratios in the HCNH<sup>+</sup> images, we only estimate the excitation temperatures toward emission peaks. Toward bolo12 and bolo4 in the Serpens filament, we obtain excitation temperatures of  $\sim 7$  K and  $\sim 18$  K, respectively. Toward KAM280, we convolve the HCNH<sup>+</sup> (2–1) raw data of Serpens South to an angular resolution of 27'' to match the angular resolution of the HCNH<sup>+</sup> (3–2) spectra, and then derive the line ratio which indicates an excitation temperature of  $\sim 12$  K. The integrated intensity ratio between HCNH<sup>+</sup> (2–1) and HCNH<sup>+</sup> (1–0) is  $\sim 2$  in the averaged spectra (see Fig. 4), corresponding to an excitation temperature of  $\sim 10$  K. The excitation temperatures are close to the gas kinetic temperature derived from ammonia (e.g., Friesen et al. 2016). These estimates imply that the excitation temperatures might vary within the range of 7–18 K. In

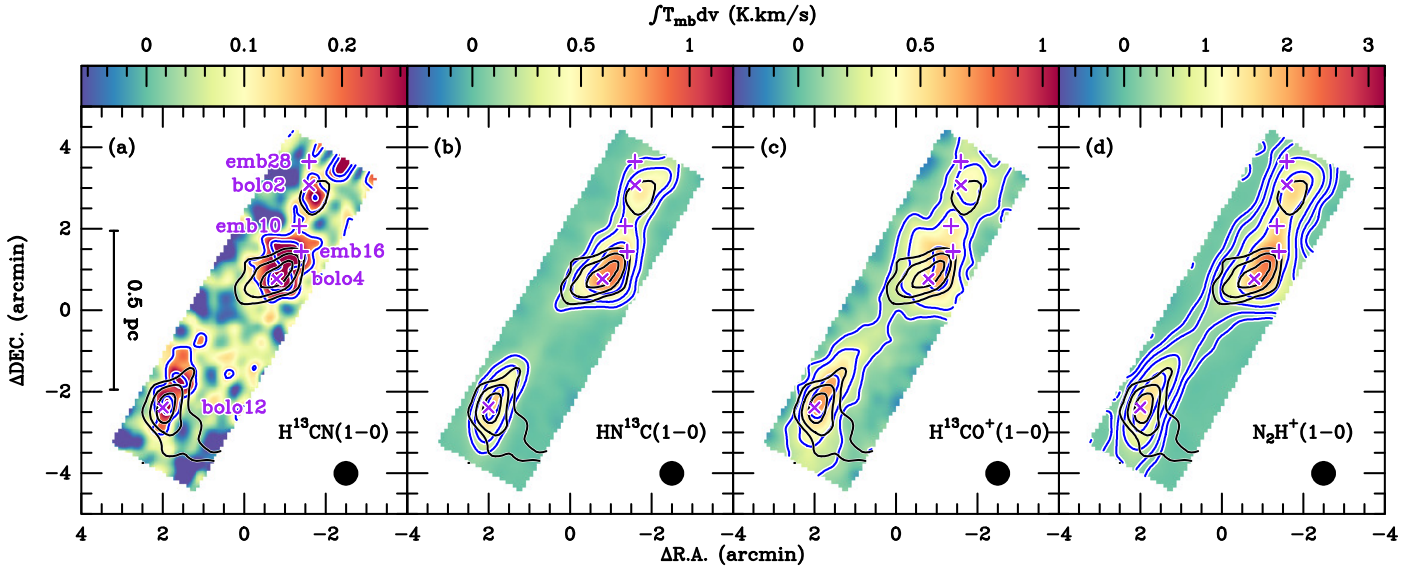


**Fig. 5.** Comparison of different tracers in the Serpens filament. Integrated-intensity maps (in color scale) of (a)  $\text{H}^{13}\text{CN}$  (1–0), (b)  $\text{HN}^{13}\text{C}$  (1–0), (c)  $\text{H}^{13}\text{CO}^+$  (1–0), and (d)  $\text{N}_2\text{H}^+$  (1–0). The blue contours represent the respective integrated intensities that are  $2'' \times 0.15 \text{ K km s}^{-1}$  and  $n = 0, 1, 2, \dots$ . The black contours of  $\text{HCNH}^+$  (2–1) integrated intensities are the same as in Fig. 1a. The intensity was integrated over  $7\text{--}9.5 \text{ km s}^{-1}$  for  $\text{HN}^{13}\text{C}$  (1–0), and  $\text{H}^{13}\text{CO}^+$  (1–0), while a broader velocity range ( $5\text{--}9.5 \text{ km s}^{-1}$ ) was chosen to cover the three main HFS components of  $\text{N}_2\text{H}^+$  (1–0). The beam size is shown in the lower right corner of each panel. In all panels, the (0, 0) offset corresponds to  $\alpha_{\text{J2000}}=18^{\text{h}}28^{\text{m}}50^{\text{s}}.4$ ,  $\delta_{\text{J2000}}=00^{\circ}49'58''.72$ . The markers are the same as in Fig. 1.

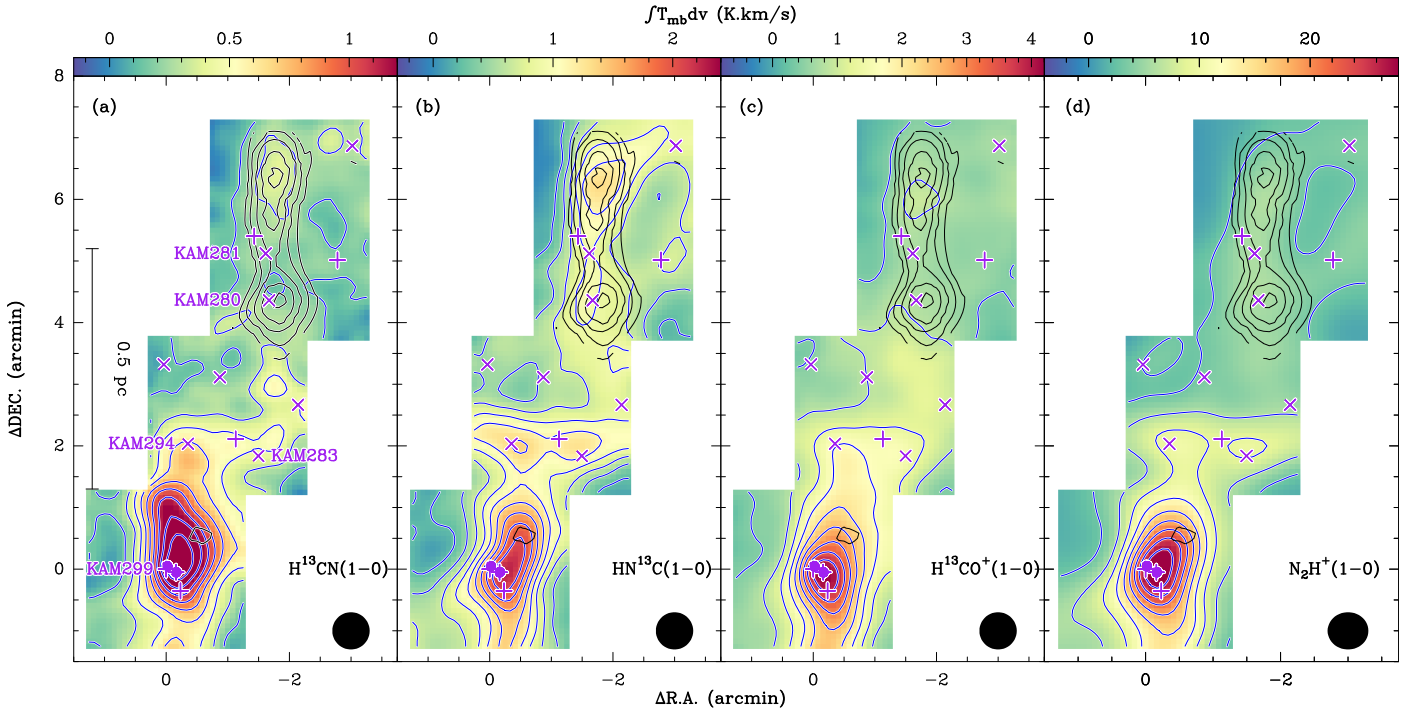


**Fig. 6.** Comparison of different tracers in Serpens South. Integrated-intensity maps (in color scale) of (a)  $\text{H}^{13}\text{CN}$  (1–0), (b)  $\text{HN}^{13}\text{C}$  (1–0), (c)  $\text{H}^{13}\text{CO}^+$  (1–0), and (d)  $\text{N}_2\text{H}^+$  (1–0). The blue contours represent the respective integrated intensities. They vary from 10% to 90% of the peak integrated intensities in steps of 10%, where the peak integrated intensities are  $1.57 \text{ K km s}^{-1}$ ,  $2.25 \text{ K km s}^{-1}$ ,  $4.26 \text{ K km s}^{-1}$ , and  $30.24 \text{ K km s}^{-1}$  for  $\text{H}^{13}\text{CN}$  (1–0),  $\text{HN}^{13}\text{C}$  (1–0),  $\text{H}^{13}\text{CO}^+$  (1–0), and  $\text{N}_2\text{H}^+$  (1–0), respectively. The black contours of  $\text{HCNH}^+$  (2–1) integrated intensities are the same as in Fig. 2a. The intensity was integrated over  $7\text{--}9.5 \text{ km s}^{-1}$  for  $\text{H}^{13}\text{CN}$  (1–0),  $\text{HN}^{13}\text{C}$  (1–0), and  $\text{H}^{13}\text{CO}^+$  (1–0), while a broader range ( $5\text{--}9.5 \text{ km s}^{-1}$ ) was chosen to cover the three main HFS components of  $\text{N}_2\text{H}^+$  (1–0). The beam size is shown in the lower right corner of each panel. In all panels, the (0, 0) offset corresponds to  $\alpha_{\text{J2000}}=18^{\text{h}}30^{\text{m}}04^{\text{s}}.19$ ,  $\delta_{\text{J2000}}=-02^{\circ}03'05''.5$ . The markers are the same as in Fig. 2.

the following analysis, we assume a constant excitation temperature of  $12 \text{ K}$  in order to derive the column density of  $\text{HCNH}^+$ .

Considering an excitation temperature range of  $7\text{--}18 \text{ K}$ , the assumption of a fixed excitation temperature can introduce uncer-



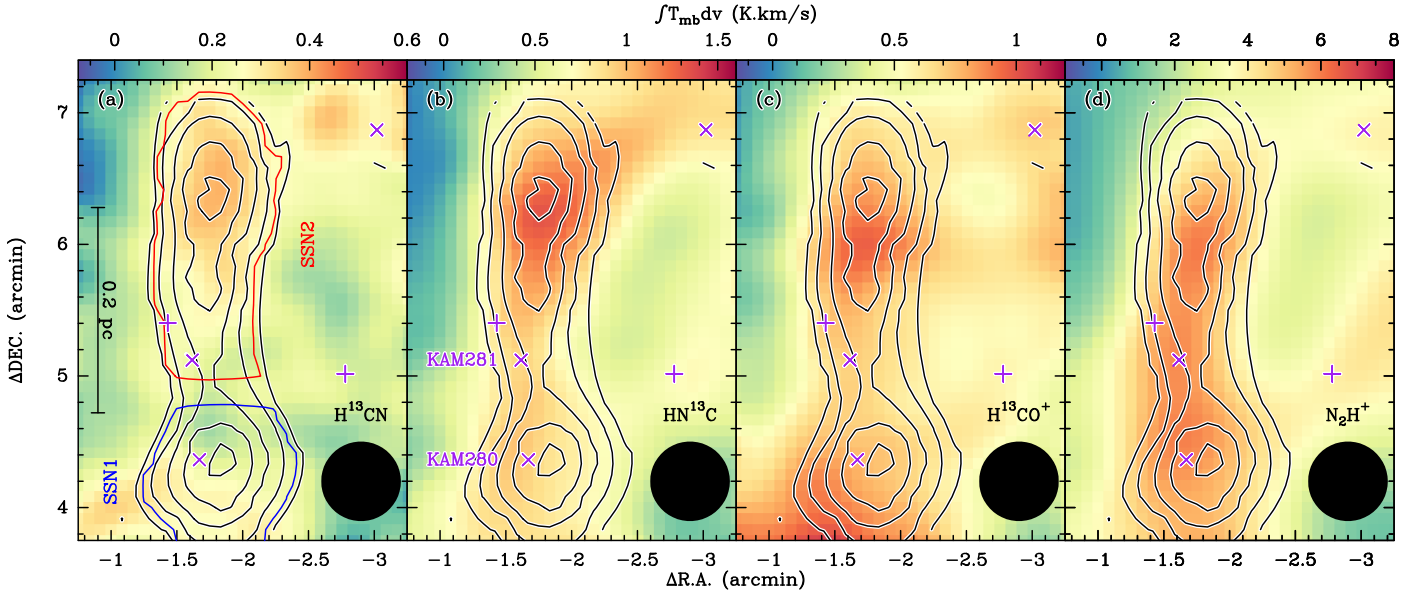


**Fig. 7.** Same as Fig. 6 but zoomed in on SSN with different color scales for better visualization. The two subregions, SSN1 and SSN2, are labeled in panel (a).

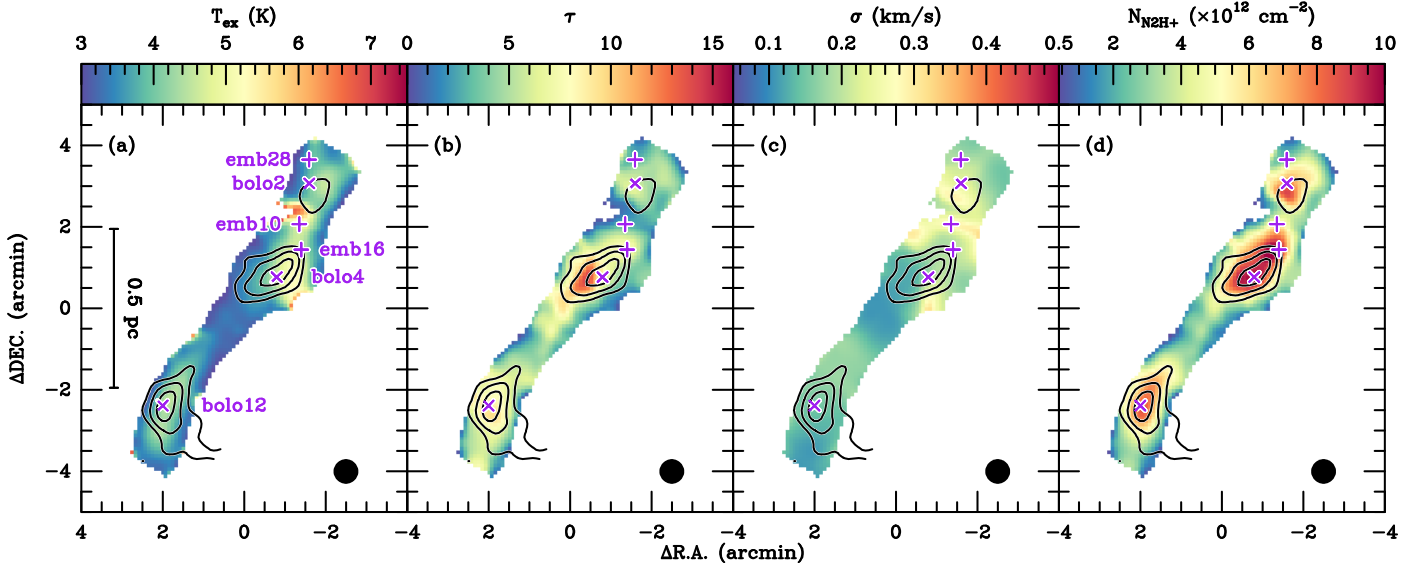


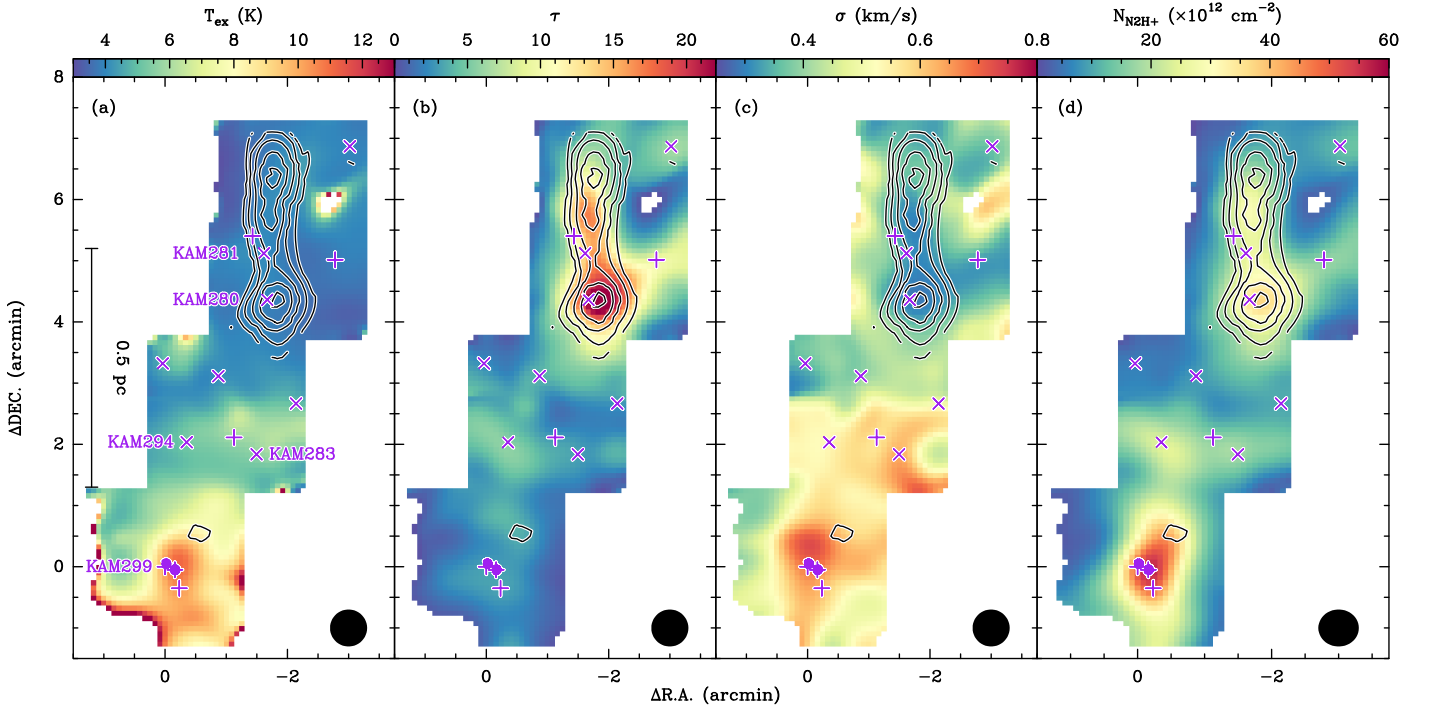
**Fig. 8.** Distributions (a)  $N_2H^+$  (1–0) excitation temperature, (b) total optical depth, (c) velocity dispersion, and (d)  $N_2H^+$  column density toward the Serpens filament. The overlaid  $HCNH^+$  (2–1) integrated-intensity contours are the same as in Fig. 1a.

tainties in the derived  $HCNH^+$  column densities of at most 15%. Making use of the excitation temperature, we made a fit to the  $HCNH^+$  (3–2) data of KAM299 in Fig. 10, which demonstrates that our sensitivities are not sufficient to detect  $HCNH^+$  (1–0) and (2–1).

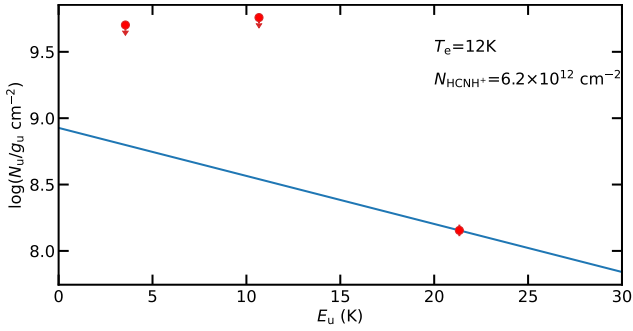
Because  $H^{13}CN$  (1–0),  $HN^{13}C$  (1–0), and  $H^{13}CO^+$  (1–0) have quite high critical densities (see Table 1), these transitions are likely sub-thermal. Hence, we adopt a lower excitation temperature of 5 K for  $H^{13}CN$  (1–0),  $HN^{13}C$  (1–0), and  $H^{13}CO^+$  (1–0). This assumption is consistent with the excitation temperature assumed for these species in previous studies toward dark clouds (e.g., Hirota et al. 1998). If the excitation temperature is as high as 10 K, the derived column densities are underestimated by only  $\sim 6\%$  for  $H^{13}CN$ ,  $HN^{13}C$ , and  $H^{13}CO^+$ . Using the assumed excitation temperatures, we can calculate the column densities of  $HCNH^+$ ,  $H^{13}CN$ ,  $HN^{13}C$ , and  $H^{13}CO^+$  from

$HCNH^+$  (2–1),  $H^{13}CN$  (1–0),  $HN^{13}C$  (1–0), and  $H^{13}CO^+$  (1–0), respectively. The distributions of these molecular column densities are shown in Appendix A. The derived column densities are listed in Table 3, where the errors were estimated through a Monte Carlo analysis. In this analysis, we estimate the uncertainties in the column densities derived by generating 10,000 realizations randomly sampled from the Gaussian distributions associated with integrated intensities, optical depths, and line widths, propagating these samples through through Eq. (9), and then analyzing the resulting distribution of outcomes to estimate the uncertainties.

Molecular abundances,  $X(A) = N(A)/N(H_2)$ , are derived from the ratio between molecular column densities,  $N(A)$ , and  $H_2$  column densities,  $N(H_2)$ , by adopting the *Herschel* dust-based  $H_2$  column density maps (Könyves et al. 2015; Fiorellino et al. 2021). The derived molecular abundances are listed in



**Fig. 9.** Distribution of (a)  $\text{N}_2\text{H}^+$  (1–0) excitation temperature, (b) total optical depth, (c) velocity dispersion, and (d)  $\text{N}_2\text{H}^+$  column density toward Serpens South. The red pixels at the southern boundary of panel a have large uncertainties in the fitted excitation temperatures. The overlaid  $\text{HCNH}^+$  (2–1) integrated-intensity contours are the same as in Fig. 2a.



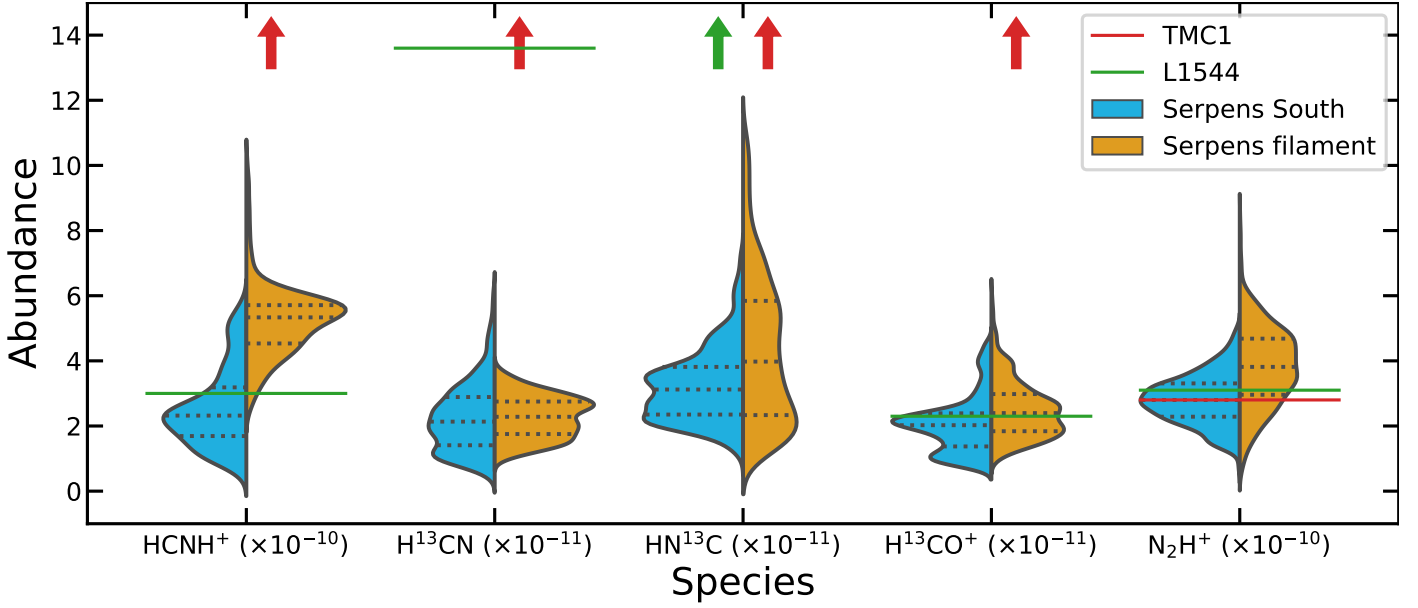
**Fig. 10.** Population diagram of  $\text{HCNH}^+$  toward KAM299. The blue line represents the fit expected from the excitation temperature and  $\text{HCNH}^+$  column density which are indicated in the top right corner.

Table 4, and the statistical results of the derived molecular abundances are presented in Fig. 11. Compared to TMC1 and L1544 (Caselli et al. 2002a,b; Agúndez & Wakelam 2013; Quénard et al. 2017; Hirota et al. 1998), we find that the  $\text{H}^{13}\text{CN}$ ,  $\text{HN}^{13}\text{C}$ , and  $\text{H}^{13}\text{CO}^+$  abundances are lower in Serpens South and the Serpens filament (see Fig. 11). On the other hand, the derived  $\text{N}_2\text{H}^+$  abundances in TMC1 and L1544 are comparable to those of our mapped regions, which suggests that  $\text{N}_2\text{H}^+$  abundances do not vary much in different environments. For  $\text{HCNH}^+$ , the molecular abundances vary from  $6.5 \times 10^{-11}$  to  $5.9 \times 10^{-10}$  with a median value of  $2.4 \times 10^{-10}$  and  $5.6 \times 10^{-10}$  in Serpens South and the Serpens filament, respectively. These values are comparable to that in L1544 ( $\sim 3 \times 10^{-10}$ , Quénard et al. 2017) but lower than that of TMC1 ( $\sim 1.9 \times 10^{-9}$ , Schilke et al. 1991) and generally higher than the abundances measured in high-mass star formation regions ( $0.9\text{--}14 \times 10^{-11}$ , Fontani et al. 2021).

We further investigate the  $\text{HCNH}^+$  abundance variation as a function of evolutionary stage in Fig. 12, which suggests that the  $\text{HCNH}^+$  abundance decreases by almost two orders of magnitude from the starless phase to the protostellar phase. This finding is consistent with the results toward high-mass star formation regions where the decrease in the  $\text{HCNH}^+$  abundance is attributed to an evolutionary effect (Fontani et al. 2021).

The spatial distributions of molecular fractional abundances are shown in Figs. 13 and 14. In Fig. 13,  $\text{H}^{13}\text{CO}^+$  abundances peak toward the west of the dust continuum peak in bolo4. In contrast,  $\text{HCNH}^+$ ,  $\text{HN}^{13}\text{C}$ ,  $\text{H}^{13}\text{CN}$ , and  $\text{N}_2\text{H}^+$  can still trace the core center of bolo4. It is expected that  $\text{H}^{13}\text{CO}^+$  would not be a reliable tracer of the core center in bolo4, as CO, which is a main precursor of  $\text{HCO}^+$ , has been observed to undergo depletion in this region (Gong et al. 2018, 2021). This is consistent with the fact that CO freezes out onto dust grains for cold and dense regions.

In Fig. 14, we find that the molecular fractional abundances of  $\text{HCNH}^+$ ,  $\text{H}^{13}\text{CN}$ ,  $\text{HN}^{13}\text{C}$ ,  $\text{H}^{13}\text{CO}^+$  are lower in the southern part of SSN2 than the northern part of SSN2 by a factor of  $\geq 2$ , which suggests a north-south abundance gradient across SSN2. The  $\text{H}^{13}\text{CN}$ ,  $\text{HN}^{13}\text{C}$ ,  $\text{H}^{13}\text{CO}^+$  abundances are even lower in SSN1. This could be caused by the freeze-out process on to dust grains that affects these molecules or their main precursor molecules. For  $\text{H}^{13}\text{CN}$ ,  $\text{HN}^{13}\text{C}$ ,  $\text{H}^{13}\text{CO}^+$ , the depletion sizes are found to be  $\sim 0.3$  pc. In contrast,  $\text{N}_2\text{H}^+$  and  $\text{NH}_3$  appear to still be abundant in SSN, which supports the selective freeze-out whereby molecules exhibit different behaviors when interacting with dust grains (e.g., Bergin & Tafalla 2007). Our results are roughly in line with the scenario that CO is the first to be depleted, followed by HCN, HNC, and  $\text{HCNH}^+$ , while  $\text{NH}_3$  and  $\text{N}_2\text{H}^+$  are least affected. We also notice that even  $\text{N}_2\text{H}^+$  abundances appear to drop toward the peak of the SSC when compared to ambient gas, which is similar to  $\text{NH}_3$  (Friesen et al.



**Fig. 11.** Comparison of the fractional abundances of different species with respect to  $H_2$  determined on a pixel-by-pixel basis. The y-axis has been divided by the scaling values which are given in parentheses after the molecule names along the x-axis for better visualization. The dotted lines indicate the 25%, 50%, and 75% percentiles of the respective distributions. The molecular abundances in TMC1 and L1544 are also indicated for comparison. The arrows indicate that their abundances are higher than the maximum value in the y-axis.

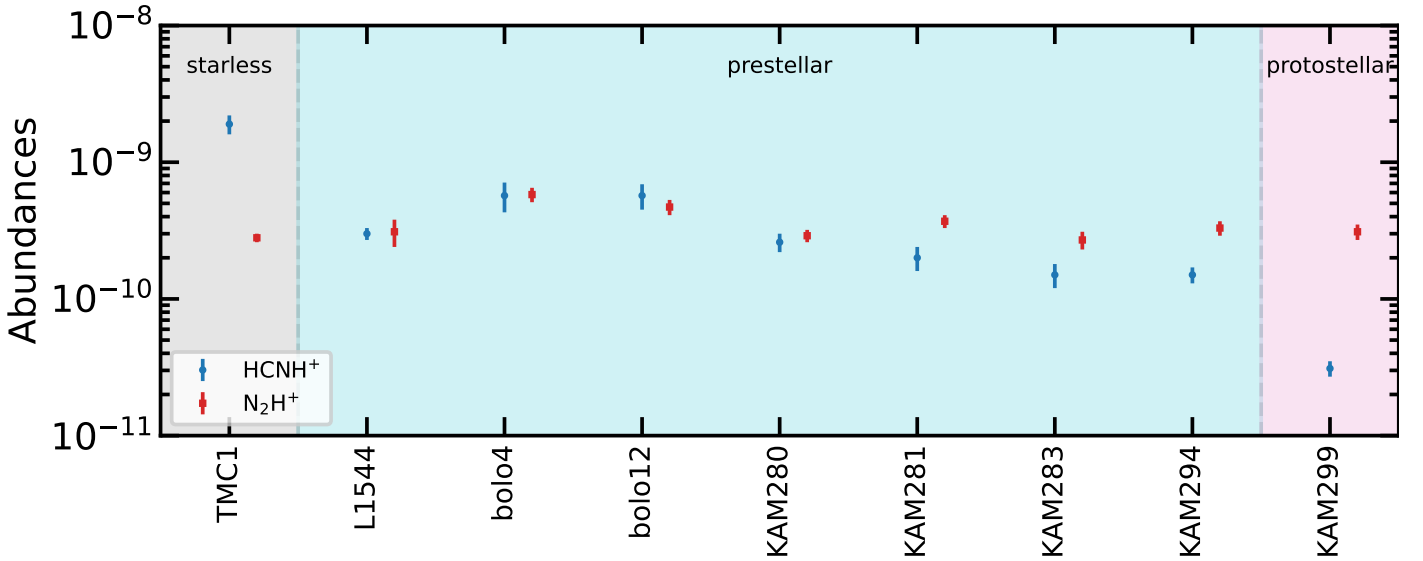
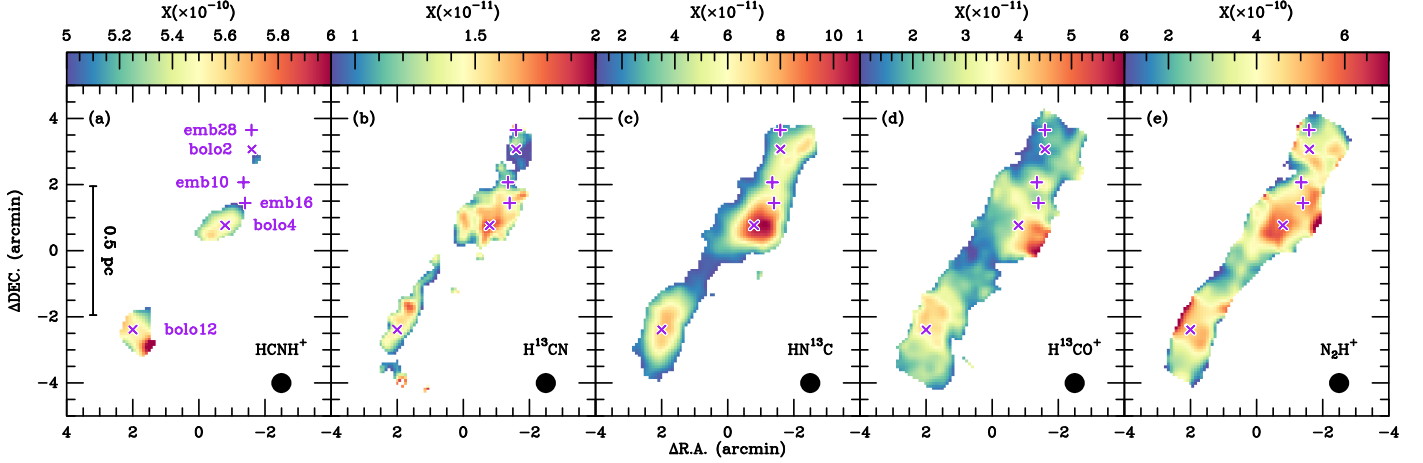


**Fig. 12.**  $HCNH^+$  (blue) and  $N_2H^+$  (red) abundances relative to  $H_2$  as a function of evolutionary stages.

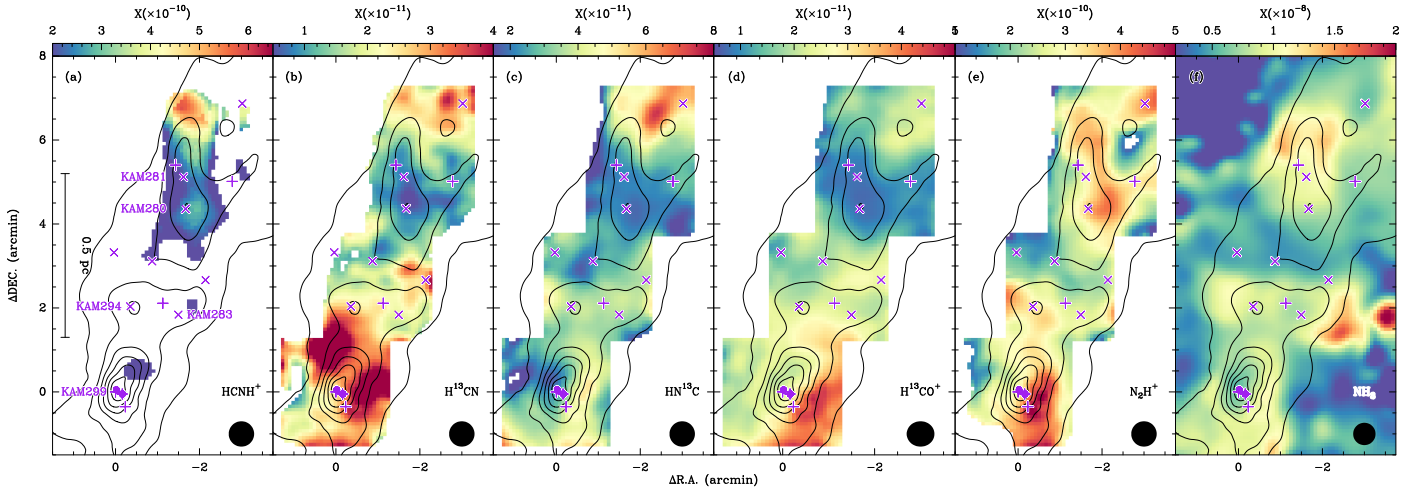
2016). Such low abundances indicate that even  $N_2H^+$  and  $NH_3$  begin to deplete from the gas phase in SSC (Bergin et al. 2002; Belloche & André 2004; Bergin & Tafalla 2007). Another potential scenario is that the elevated kinetic temperatures within the SSC lead to CO desorption back to the gas phase, facilitating the efficient destruction of  $N_2H^+$ . This phenomenon would also trigger the desorption of  $NH_3$  back to the gas phase, potentially enriching its abundances. However, the  $NH_3$  abundance remains relatively low within the SSC, which might be attributed to the inefficient  $NH_3$  desorption.

Figure 15 shows the pixel-by-pixel comparison of the abundances of  $HCNH^+$  and the other five molecules. It is evident that  $H^{13}CO^+$ ,  $H^{13}CN$ , and  $HN^{13}C$  abundances generally increase with increasing  $HCNH^+$  abundances toward SSN2, SSC, bolo4,

and bolo12. This can be readily explained by the freeze-out of CO, HCN, and HNC. However, we find that SSN1 exhibits the opposite trend where the  $H^{13}CO^+$ ,  $H^{13}CN$ , and  $HN^{13}C$  abundances generally decrease with increasing  $HCNH^+$  abundances. Instead,  $HCNH^+$  abundances are positively correlated with  $N_2H^+$  and  $NH_3$  in SSN1, in agreement with the spatially coincident distribution of  $HCNH^+$  and  $N_2H^+$  as shown in Fig. 14. This implies a different chemical formation pathway for  $HCNH^+$  in SSN1 (details are discussed in Sect. 4.2). We also find that SSC forms a distinct group in this figure, especially from the comparison of  $HCNH^+$  with  $H^{13}CO^+$  and  $H^{13}CN$ . The abundance ratios of  $X(HCNH^+)/X(H^{13}CO^+)$  and  $X(HCNH^+)/X(H^{13}CN)$  are  $\lesssim 5$  in SSC, which are much lower than in other regions. This trend is similar to the results of Fontani et al. (2021)



**Fig. 13.** Molecular abundance distributions of  $\text{HCNH}^+$  (panel a),  $\text{H}^{13}\text{CN}$  (panel b),  $\text{HN}^{13}\text{C}$  (panel c),  $\text{H}^{13}\text{CO}^+$  (panel d), and  $\text{N}_2\text{H}^+$  (panel e) in the Serpens filament. The beam size is shown in the lower right corner of each panel. In all panels, the (0, 0) offset corresponds to  $\alpha_{J2000}=18^{\text{h}}28^{\text{m}}50^{\text{s}}.4$ ,  $\delta_{J2000}=00^{\circ}49'58''.72$ . The markers are the same as in Fig. 1.



**Fig. 14.** Molecular abundance distributions of  $\text{HCNH}^+$  (panel a),  $\text{H}^{13}\text{CN}$  (panel b),  $\text{HN}^{13}\text{C}$  (panel c),  $\text{H}^{13}\text{CO}^+$  (panel d),  $\text{N}_2\text{H}^+$  (panel e), and para- $\text{NH}_3$  (panel f, from Friesen et al. 2016) in Serpens South. The overlaid *Herschel* dust-based  $\text{H}_2$  column density contours start at  $2.4 \times 10^{22} \text{ cm}^{-2}$  and increase by  $2.4 \times 10^{22} \text{ cm}^{-2}$ . The beam size is shown in the lower right corner of each panel. In all panels, the (0, 0) offset corresponds to  $\alpha_{J2000}=18^{\text{h}}30^{\text{m}}04^{\text{s}}.19$ ,  $\delta_{J2000}=-02^{\circ}03'05''.5$ . The markers are the same as in Fig. 2.

where warmer sources have lower  $X(\text{HCNH}^+)/X(\text{HCO}^+)$  and  $X(\text{HCNH}^+)/X(\text{HCN})$  ratios. This can be attributed to the elevated kinetic temperatures which in turn enhance the  $\text{H}^{13}\text{CO}^+$  and  $\text{H}^{13}\text{CN}$  abundances.

## 4. Discussion

### 4.1. Environmental dependence

As shown in Sect. 3.2, molecular abundances are sensitive to environmental conditions. Here, we attempt to quantify how the observed abundances depend on the physical parameters.

Figure 16 presents the comparison between the derived molecular abundances and  $\text{H}_2$  column densities for the five molecules. In contrast to other molecules, the abundance of  $\text{HCNH}^+$  shows an overall anti-correlation with  $\text{H}_2$  column density with a strongly negative Pearson correlation coefficient of  $-0.73$ . This further supports that  $\text{HCNH}^+$  is abundant in low-density regions. It is also evident that the  $\text{H}^{13}\text{CO}^+$ ,  $\text{H}^{13}\text{CN}$ ,  $\text{HN}^{13}\text{C}$ , and  $\text{HCNH}^+$  abundances decrease with increasing  $\text{H}_2$  column density toward SSN. This pattern aligns with the depletion

caused by the freeze-out process of  $\text{CO}$ ,  $\text{HCN}$ , and  $\text{HNC}$ . Given that these molecules are known to be the main precursors of  $\text{HCO}^+$  and  $\text{HCNH}^+$ , the freeze-out process causes the depletion of  $\text{HCO}^+$  and  $\text{HCNH}^+$ . Interestingly,  $\text{HCNH}^+$  has a lower abundance in SSC than in SSN. In contrast,  $\text{HCO}^+$  and  $\text{HCN}$  are more abundant in SSC than in SSN, which could be potentially explained by the thermal desorption of  $\text{CO}$ ,  $\text{H}_2\text{O}$ , and  $\text{HCN}$  from dust grains to the gas phase. Such desorption can be caused by elevated kinetic temperatures, for example due to outflow shocks. However, such a desorption process seems not to enhance the  $\text{HCNH}^+$  abundance in SSC.

In order to investigate the dependence of molecular abundances on gas kinetic temperature, we make use of the gas kinetic temperature derived from ammonia inversion transitions. Because of the lack of a gas kinetic temperature map toward the Serpens filament, we only investigate the molecular abundance variation as a function of the gas kinetic temperature toward Serpens South, which is shown in Fig. 17. Overall, the  $\text{H}^{13}\text{CO}^+$  and  $\text{H}^{13}\text{CN}$  abundances increase with increasing kinetic temperatures, while that of  $\text{HCNH}^+$  shows an opposite trend.

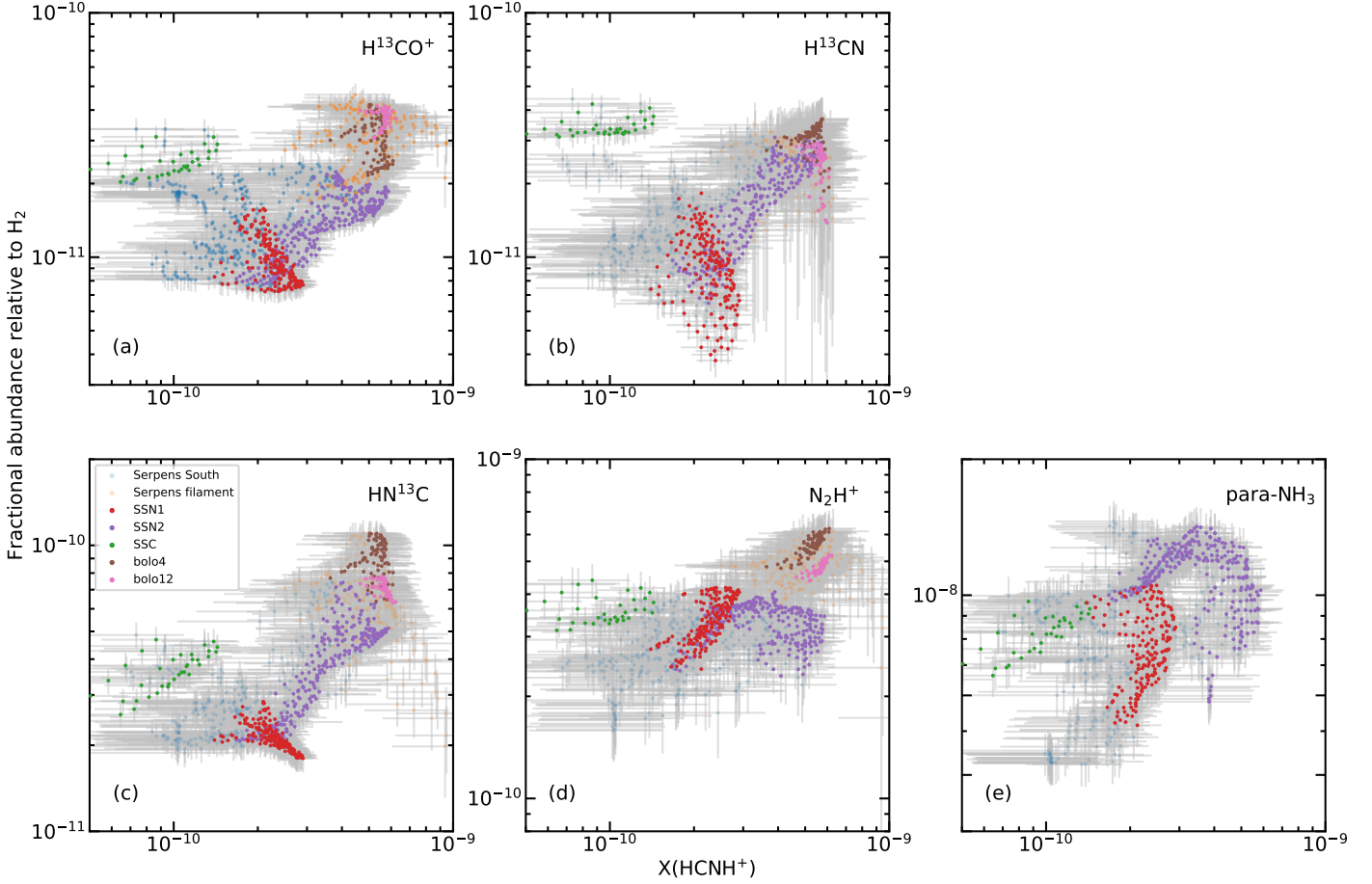


**Fig. 15.** Pixel-by-pixel comparison of the abundances of  $\text{HCNH}^+$  and the other five molecules in the Serpens filament and Serpens South. The corresponding molecule is indicated in the upper right corner of each panel. The subregions are indicated by the different colors in the legend of panel c.

**Table 3.** Molecular column densities of the observed targets.

Name	$T_d$ (K)	$T_g$ (K)	$N(\text{H}_2)$ ( $\times 10^{22} \text{ cm}^{-2}$ )	$N(\text{HCNH}^+)^*$ ( $\times 10^{12} \text{ cm}^{-2}$ )	$N(\text{H}^{13}\text{CN})^*$ ( $\times 10^{11} \text{ cm}^{-2}$ )	$N(\text{HN}^{13}\text{C})^*$ ( $\times 10^{11} \text{ cm}^{-2}$ )	$N(\text{H}^{13}\text{CO}^+)^*$ ( $\times 10^{11} \text{ cm}^{-2}$ )	$N(\text{N}_2\text{H}^+)$ ( $\times 10^{12} \text{ cm}^{-2}$ )
(1)	(2)	(3)	(4)	(5)	(6)	(7)	(8)	(9)
The Serpens filament	12.0–16.3	...	0.3–2.2	5.1–10.3	1.1–6.3	0.7–18.2	0.6–7.0	0.4–10.8
bolo4	12.4	...	1.7	9.7 $\pm$ 2.1	6.1 $\pm$ 1.1	17.9 $\pm$ 0.3	5.8 $\pm$ 0.2	10.0 $\pm$ 0.7
bolo12	12.5	...	1.8	10.1 $\pm$ 1.8	4.7 $\pm$ 0.5	12.9 $\pm$ 0.1	6.7 $\pm$ 0.2	8.3 $\pm$ 0.5
Serpens South	11.1–16.5	10.3–17.5	1.8–16.7	4.2–27.1	2.5–46.8	1.9–45.0	1.1–41.2	0.8–57.1
KAM280	11.4	10.9	9.6	24.8 $\pm$ 2.3	6.3 $\pm$ 0.3	18.7 $\pm$ 0.3	7.5 $\pm$ 0.2	35.1 $\pm$ 2.0
KAM281	11.6	10.7	8.6	17.1 $\pm$ 2.4	6.7 $\pm$ 0.4	18.0 $\pm$ 0.3	6.8 $\pm$ 0.1	24.7 $\pm$ 1.5
KAM283	12.4	12.6	6.6	10.8 $\pm$ 1.8	12.9 $\pm$ 0.4	23.2 $\pm$ 0.5	14.6 $\pm$ 0.3	17.7 $\pm$ 1.4
KAM294	13.4	12.9	7.3	12.6 $\pm$ 1.3	20.1 $\pm$ 0.4	26.8 $\pm$ 0.5	16.2 $\pm$ 0.2	23.9 $\pm$ 1.4
KAM299	16.0	16.4	16.4	6.2 $\pm$ 0.5	42.2 $\pm$ 0.3	37.3 $\pm$ 0.9	37.3 $\pm$ 0.9	50.6 $\pm$ 2.2

**Notes.** (1) Source name. (2) Dust temperature. (3) Gas kinetic temperature. “...” indicates that no information is available. (4)  $\text{H}_2$  column density. (5)  $\text{HCNH}^+$  column density. For KAM283, KAM294, and KAM299 where  $\text{HCNH}^+$  (2–1) emission is not detected, we use  $\text{HCNH}^+$  (3–2) to estimate the column densities at a resolution of  $27''$ . (6)  $\text{H}^{13}\text{CN}$  column density. (7)  $\text{HN}^{13}\text{C}$  column density. (8)  $\text{H}^{13}\text{CO}^+$  column density. (9)  $\text{N}_2\text{H}^+$  column density. “\*\*\*” indicates that these column densities are derived under the optically thin assumption. A constant excitation temperature of 12 K is assumed for  $\text{HCNH}^+$ , while a constant excitation temperature of 5 K is assumed for  $\text{H}^{13}\text{CN}$ ,  $\text{HN}^{13}\text{C}$ , and  $\text{H}^{13}\text{CO}^+$ .

$\text{HN}^{13}\text{C}$  and  $\text{N}_2\text{H}^+$  appear to be the least affected by variation in the kinetic temperature. Toward the SSC,  $\text{H}^{13}\text{CO}^+$ ,  $\text{HN}^{13}\text{C}$ ,  $\text{HCNH}^+$ , and  $\text{N}_2\text{H}^+$  exhibit a different behavior from  $\text{H}^{13}\text{CN}$  whose molecular abundances appear to increase with increasing kinetic temperature. The different behaviors between  $\text{H}^{13}\text{CN}$  and  $\text{HN}^{13}\text{C}$  could be explained by the fact that  $\text{HCN}/\text{HNC}$  abundance ratio increases with kinetic temperature (e.g., Hacar et al.

2020). However, the gas kinetic temperature range (14–17 K) is too narrow to reach a more concrete conclusion.

**Table 4.** Molecular abundances with respect to H<sub>2</sub> toward different targets.

Name	$X(\text{HCNH}^+)$ ( $\times 10^{-10}$ )	$X(\text{H}^{13}\text{CN})$ ( $\times 10^{-11}$ )	$X(\text{HN}^{13}\text{C})$ ( $\times 10^{-11}$ )	$X(\text{H}^{13}\text{CO}^+)$ ( $\times 10^{-11}$ )	$X(\text{N}_2\text{H}^+)$ ( $\times 10^{-10}$ )
(1)	(2)	(3)	(4)	(5)	(6)
The Serpens filament	2.5–10.1	1.3–3.8	0.9–11.0	(0.9–6.1)	0.6–8.6
bolo4	5.7±1.4	3.6±0.8	10.5±0.1	3.4±0.4	5.8 ± 0.7
bolo12	5.7±1.2	2.7±0.4	7.2±0.8	3.8±0.4	4.7 ± 0.6
Serpens South	0.3–5.9	0.4–3.7	0.9–7.4	0.7–4.7	0.5–5.2
KAM280	2.6±0.4	0.7±0.1	2.0±0.2	0.8±0.1	2.9±0.3
KAM281	2.0±0.4	0.8±0.1	2.1±0.2	0.8±0.1	3.7±0.4
KAM283	1.5±0.3	2.0±0.2	3.5±0.4	2.2±0.2	2.7±0.4
KAM294	1.5±0.2	2.7±0.3	3.7±0.4	2.2±0.2	3.3±0.4
KAM299	0.31±0.04	2.6±0.3	2.3±0.2	2.3±0.2	3.1±0.4
TMC1	19.0±3.0	17.8±2.1	41.7±6.2	14.4±0.3	2.8±0.2
L1544	3.0±0.3	13.6±1.7	31.4±5.7	2.3±0.7	3.1±0.7

**Notes.** (1) Source name. (2) HCNH<sup>+</sup> fractional abundance relative to H<sub>2</sub>. (3) H<sup>13</sup>CN fractional abundance relative to H<sub>2</sub>. (4) HN<sup>13</sup>C fractional abundance relative to H<sub>2</sub>. (5) H<sup>13</sup>CO<sup>+</sup> fractional abundance relative to H<sub>2</sub>. (6) N<sub>2</sub>H<sup>+</sup> fractional abundance relative to H<sub>2</sub>. The uncertainties of molecular abundances are estimated by assuming 10% uncertainties in the dust-based H<sub>2</sub> column densities (Könyves et al. 2015). The molecular abundances in TMC1 are taken from Pratap et al. (1997) and Schilke et al. (1991), while the molecular abundances in L1544 are based on Caselli et al. (2002a), Caselli et al. (2002b), Quénard et al. (2017), and Hirota et al. (1998).

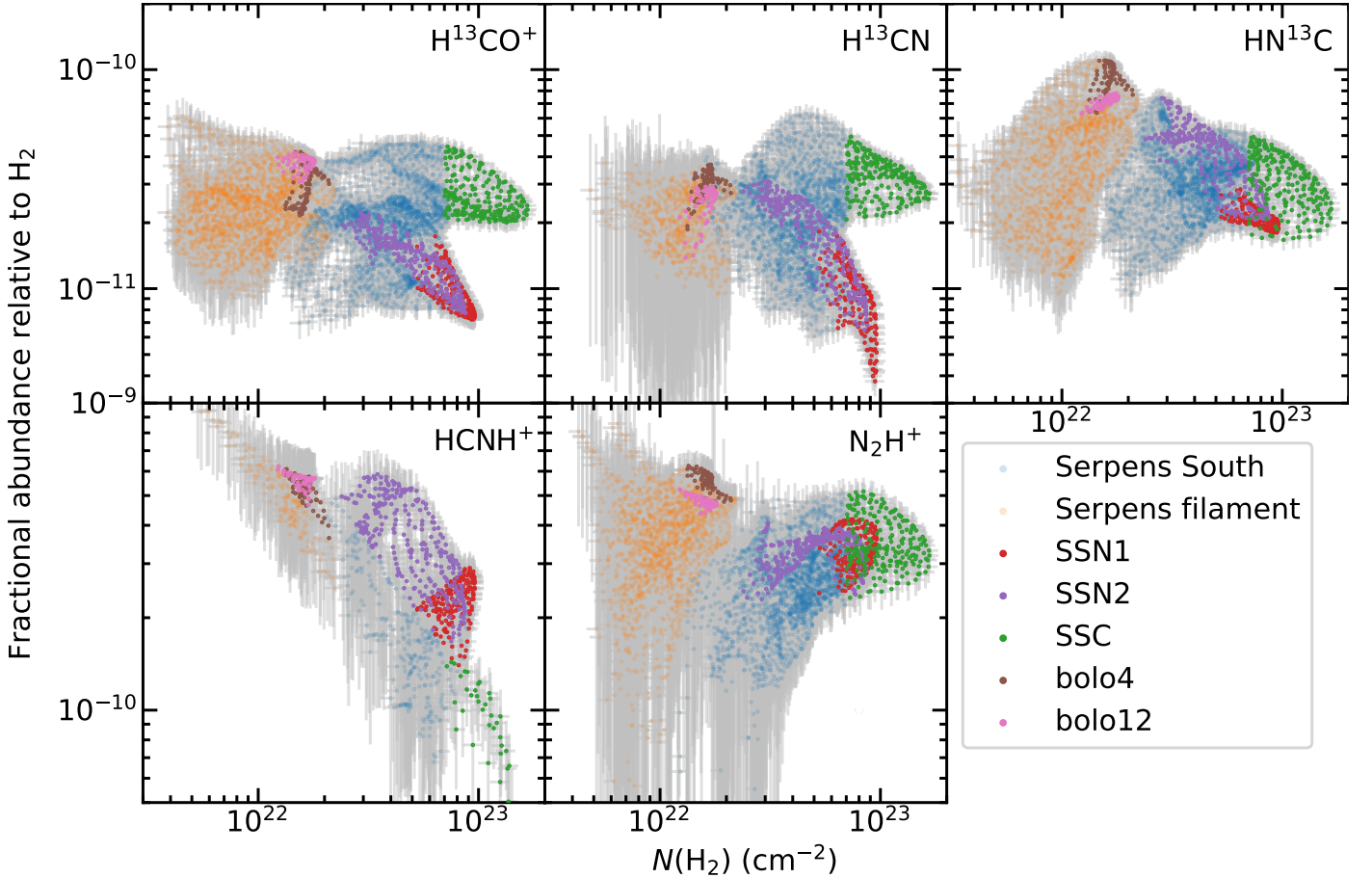


**Fig. 16.** Fractional abundances as a function of H<sub>2</sub> column density for the five molecules indicated in the top right corner of each panel. Different regions are indicated by different colors as shown in the legend.

#### 4.2. Comparison between chemical models and observations

As shown in Sect. 4.1, the HCNH<sup>+</sup> abundance appears to be anticorrelated with the H<sub>2</sub> column density and kinetic temperature, which indicates that the HCNH<sup>+</sup> abundance deficit could

be caused by the increased H<sub>2</sub> number density and kinetic temperature.

In order to test this hypothesis, we used the time dependent gas-grain chemical code, *Chempl*<sup>12</sup> (Du 2021), to carry out as-

<sup>12</sup> <https://github.com/fjdu/chempl>

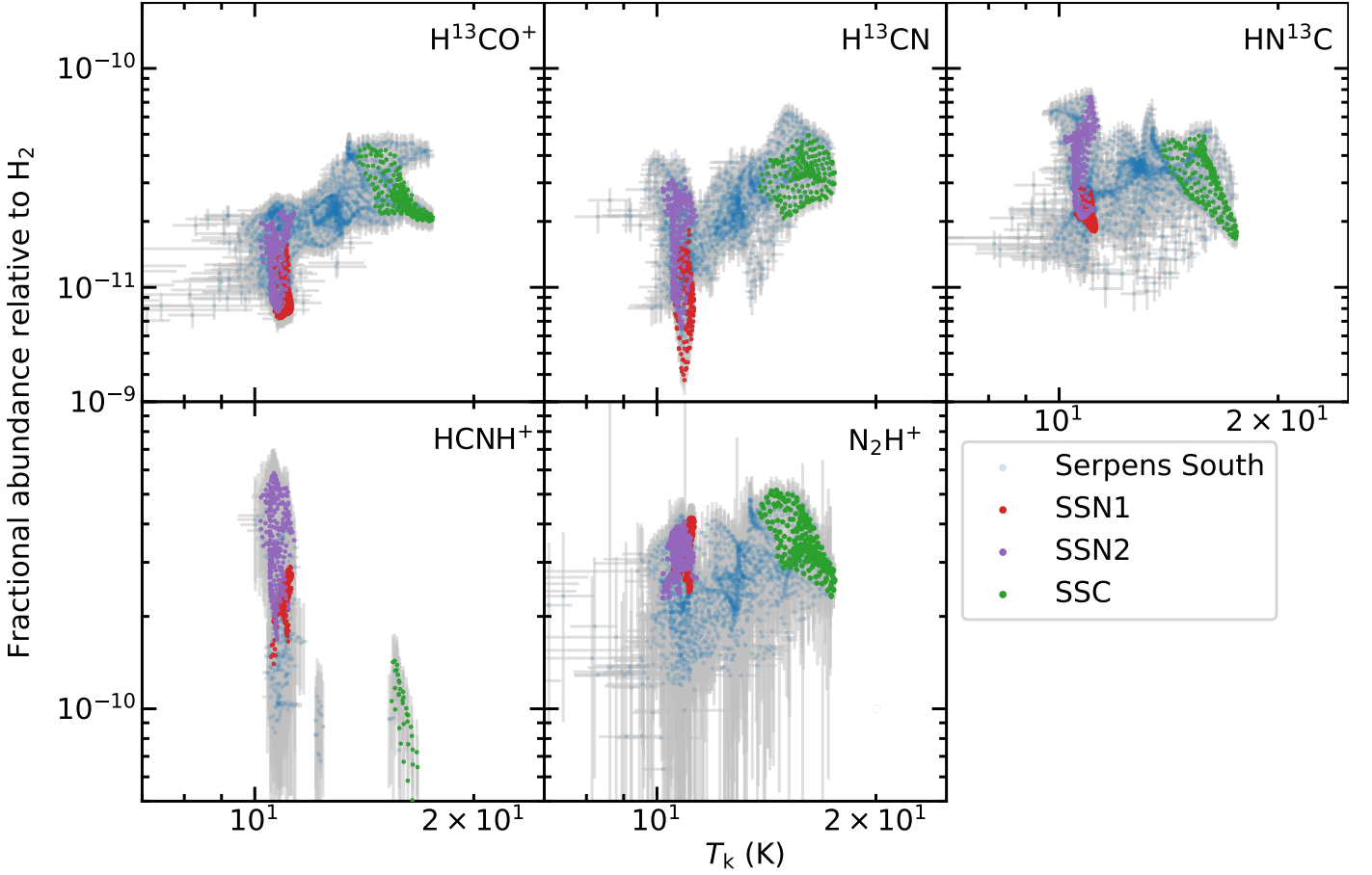


**Fig. 17.** Same as Fig. 16 but as a function of the gas kinetic temperature derived from ammonia inversion transitions.

trochemical model calculations. The UMIST RATE12 chemical network<sup>13</sup> is adopted for this study (McElroy et al. 2013). Since HCN and HNC are important precursors of HCNH<sup>+</sup>, their chemistry may also affect the chemistry of HCNH<sup>+</sup>. Two reactions are believed to be important in the chemistry of HCN and HNC in molecular clouds (e.g., Schilke et al. 1992; Talbi et al. 1996; Graninger et al. 2014; Hacar et al. 2020):



Previous studies suggest that the assumption of an energy barrier,  $\Delta E_{10}$ , of 200 K is suitable for reaction (10) (Graninger et al. 2014; Hacar et al. 2020), but quite different energy barriers  $\Delta E_{11} = 20$  K (Hacar et al. 2020) and  $\Delta E_{11} = 1125$  K (Graninger et al. 2014) have been proposed for reaction (11). Reaction (10) is included in the UMIST RATE12 chemical network, but the energy barrier is not up-to-date. On the other hand, reaction (11) is not included in the UMIST RATE12 chemical network. Hence, the two reactions with updated rate coefficients are augmented in the chemical network. The two different energy barriers of  $\Delta E_{11}$  are used for comparison in the following.

Initial conditions are needed in the chemical code for the calculations. The initial elemental abundances are the same as in Table 3 of McElroy et al. (2013), which are based on diffuse cloud values. The interstellar radiation field,  $G_0$ , is set to be  $G_0 = 1$  in Habing units (Draine 1978). Although previous studies suggest that the abundances of HCN, HNC, and HCNH<sup>+</sup> can

be regulated by the cosmic-ray ionization rate (CRIR; Fontani et al. 2021; Behrens et al. 2022), our measurements probe almost the same physical conditions and the CRIR is the same for all of the cloud volumes studied by us. Hence, we adopt the canonical value of  $1.36 \times 10^{-17} \text{ s}^{-1}$  in dense molecular gas for the CRIR (e.g., van der Tak & van Dishoeck 2000). As shown in Figs. 1–2, the HCNH<sup>+</sup> emitting regions have kinetic temperatures ranging from 10 K to 20 K and H<sub>2</sub> column densities of  $> 1 \times 10^{22} \text{ cm}^{-2}$  (i.e.,  $A_v \gtrsim 10$  mag). We use two values from the kinetic temperature, 10 K and 20 K, to investigate the effects of the kinetic temperature variations. Given their high H<sub>2</sub> column densities, our target regions are well shielded from Ultraviolet radiation. We use  $A_v = 10$  mag as a fiducial case. The modeled H<sub>2</sub> number densities are in the range of  $10^2$ – $10^6 \text{ cm}^{-3}$ .

In Fig. 18, we first compare the modeling results with  $T_g = 10$  K and  $T_g = 20$  K for a fixed H<sub>2</sub> number density of  $10^4 \text{ cm}^{-3}$ . These results suggest that the abundances change only slightly with gas temperature. This indicates that the HCNH<sup>+</sup> abundance does not significantly depend on the kinetic temperature in the range of 10–20 K. For HCNH<sup>+</sup>, the abundances are slightly higher for  $T_g = 20$  K than for  $T_g = 10$  K, which is different from Fig. 17. This is likely because the difference caused by gas temperature variation is negligible when compared to the impact of H<sub>2</sub> number densities. Hence, we mainly focus on the dependence of chemical abundances on the H<sub>2</sub> number density.

Figure 19 presents the time dependent chemical modeling results of the abundances of HCNH<sup>+</sup>, H<sup>13</sup>CN, HN<sup>13</sup>C, H<sup>13</sup>CO<sup>+</sup>, N<sub>2</sub>H<sup>+</sup> and NH<sub>3</sub>, where a <sup>12</sup>C/<sup>13</sup>C isotopic ratio of 70 is adopted to obtain the abundances of the <sup>13</sup>C-bearing molecules (e.g.,

<sup>13</sup> <http://udfa.ajmarkwick.net/>

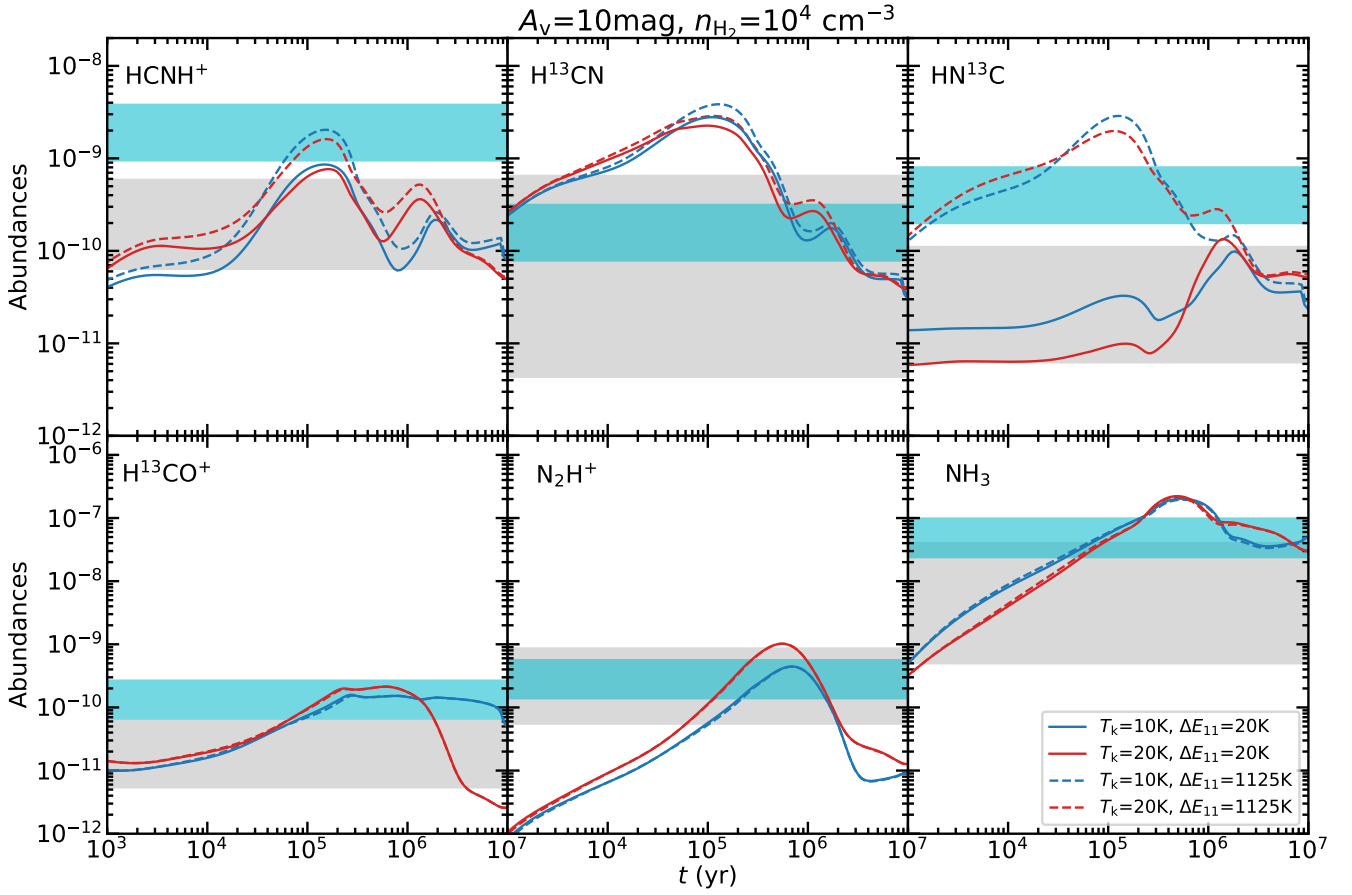


**Fig. 18.** Molecular abundances relative to  $\text{H}_2$  as a function of time, estimated from *Chempl* (Du 2021). The different colors correspond to different kinetic temperatures. The solid and dashed lines represent the modeling results with the energy barrier  $\Delta E_{11} = 20$  K and  $\Delta E_{11} = 1125$  K for reaction (11), respectively. The observed molecular abundances in our studies are indicated by the grey shaded regions, while the molecular abundances in TMC1 (Agúndez & Wakelam 2013) are indicated by the cyan shaded regions. The other physical conditions are indicated on the top of this figure.

Wilson & Rood 1994; Li et al. 2016; Yan et al. 2023) and the ortho-to-para ratio of  $\text{NH}_3$  is assumed to 4.0 (see Fig. 3 in Takano et al. 2002, for instance). We find that the two different energy barriers for reaction (11) affect the results of  $\text{HCNH}^+$ ,  $\text{H}^{13}\text{CN}$ , and  $\text{HN}^{13}\text{C}$ . The general trend is that assuming an energy barrier  $\Delta E_{11} = 1125$  K results in higher  $\text{HCNH}^+$ ,  $\text{H}^{13}\text{CN}$ , and  $\text{HN}^{13}\text{C}$  abundances than assuming  $\Delta E_{11} = 20$  K. The  $\text{HN}^{13}\text{C}$  abundances are the most significantly affected. While our observed abundances can be roughly reproduced at an  $\text{H}_2$  number density of  $10^{3-4} \text{ cm}^{-3}$  and cloud ages of around  $10^{5-6} \text{ yr}$  in Fig. 19, the high  $\text{HN}^{13}\text{C}$  abundances in TMC1 cannot be well reproduced by  $\Delta E_{11} = 20$  K suggested by Hacar et al. (2020). This indicates that the rate coefficients derived with  $\Delta E_{11} = 20$  K might not be suitable for the cold environments at  $T_g \sim 10$  K. Therefore, we only use the results with  $\Delta E_{11} = 1125$  K suggested by Graninger et al. (2014) for the following discussions.

In Figure 19, we also find that the  $\text{HCNH}^+$ ,  $\text{H}^{13}\text{CN}$ , and  $\text{HN}^{13}\text{C}$  abundances tend to reach the maximum earlier at higher  $\text{H}_2$  densities and then decrease. The timescales to reach the maximum are nearly identical for the three molecules, regardless of the  $\text{H}_2$  number densities (see also Fig. 21), indicating that  $\text{HCNH}^+$  abundances depend on the  $\text{HCN}$  and  $\text{HNC}$  abundances in the modeling results. Previous studies suggest that the reactions including Eqs. (3)–(6) are the main formation path of  $\text{HCNH}^+$  (e.g., Loison et al. 2014a; Quénard et al. 2017; Fontani et al. 2021).  $\text{HCN}$ ,  $\text{HNC}$ ,  $\text{H}_2\text{O}$ , and  $\text{HCO}^+$  are heavily depleted in

cold and dense regions (see also Sect. 3.2). Since  $\text{HCN}$  and  $\text{HNC}$  are thought to be the main precursors of  $\text{HCNH}^+$  and  $\text{HNC}^+$  (e.g., Loison et al. 2014a), these cations are also depleted in these regions. Similarly,  $\text{H}_2\text{O}$  serves as the precursor for  $\text{H}_3\text{O}^+$ , which is also expected to be depleted under these conditions. If Eqs. (3)–(6) are the main formation pathways of  $\text{HCNH}^+$ , this ion should also be depleted since its precursor molecules are heavily depleted. Therefore, the modeling results support that the decrease in its abundance is mainly caused by the freeze-out process, and the timescale of the abundance peak at a given  $\text{H}_2$  number density can be readily explained by the depletion timescale that inversely depends on the  $\text{H}_2$  number density (e.g., Caselli et al. 1999). Figure 20 presents the modeled abundances of  $\text{HCNH}^+$ ,  $\text{HCN}$ ,  $\text{HNC}$ ,  $\text{HCO}^+$ ,  $\text{N}_2\text{H}^+$  and  $\text{NH}_3$  as a function of  $\text{H}_2$  number density at a simulated timescale of  $10^6 \text{ yr}$ . This demonstrates the anti-correlation between the  $\text{H}_2$  number density and molecular abundances, which readily explains the observed  $\text{HCNH}^+$  abundance dependence of  $\text{H}_2$  column density in Fig. 16. These results suggest that  $\text{HCNH}^+$  should be the most abundant in low-density regions where precursor species like  $\text{HCN}$  and  $\text{HNC}$  do not freeze out onto dust grains. Figure 21 presents the molecular abundances reproduced by *Chempl* as a function of simulation times for the same physical conditions (i.e.,  $T_g = 10$  K,  $n_{\text{H}_2} = 10^4 \text{ cm}^{-3}$ ). This figure supports the selective freeze-out scenario in which  $\text{HCN}$  and  $\text{HNC}$  deplete earlier than  $\text{N}_2\text{H}^+$  and  $\text{NH}_3$ .



The modeling results are consistent with the observational finding that  $\text{HCNH}^+$  is the most abundant in starless cores in their early evolutionary phase. Since the density is expected to increase during gravitational collapse,  $\text{HCNH}^+$  abundances should decrease after the onset of infall. This also explains why the starless core TMC1 has a much higher  $\text{HCNH}^+$  abundance than the prestellar core L1544 and our observed regions (see Fig. 11). Investigation of  $\text{HCNH}^+$  in different evolutionary stages of low-mass star formation (see Fig. 12 and Appendix B) and non-detection of  $\text{HCNH}^+$  (3–2) around class 0 protostars (Belloche et al. 2020) are also in line with this scenario. On the other hand, mass accretion flows in SSN are indicated by previous observations (e.g., Friesen et al. 2013). Hence, we suggest that the  $\text{HCNH}^+$  abundance gradient along the SSN2 in Fig. 14a can be a result of the longitudinal mass accretion.

Although  $\text{HCNH}^+$  depletion is indeed found and appears to correlate with HCN and HNC depletion in Sect. 3.2 and Sect. 4.1, the  $\text{HCNH}^+$  abundances in SSN1 show an anticorrelation with HCN and HNC, and a positive correlation with  $\text{N}_2\text{H}^+$  and  $\text{NH}_3$ . Moreover, the  $\text{HCNH}^+$  emission peak coincides with  $\text{N}_2\text{H}^+$  emission toward SSN1. These facts imply that  $\text{HCNH}^+$  does not follow the depletion of HCN and HNC in SSN1. Such trends cannot be explained by our chemical modeling results (see Figs. 19 and 20). This suggests additional  $\text{HCNH}^+$  formation paths from molecules that do not freeze out. Because species like  $\text{NH}_3$  and  $\text{N}_2$  can still survive in the gas phase even when HCN and HNC are heavily depleted, we suggest that the ion-neutral reactions from these species become more important in the formation of  $\text{HCNH}^+$  toward freeze-out regions.

In order to further study the importance of the formation pathways for  $\text{HCNH}^+$ , we compare the rates of reactions (1)–(7). For a binary reaction, the reaction rate is defined as  $v_{\text{rate}} = kX_A X_B$ , where  $k$  is the reaction rate coefficient, and  $X_A$  and  $X_B$  are the abundances of the two reactants. However, the rate coefficients of reactions (1), (2) and (7) are not available in the RATE12 chemical network (McElroy et al. 2013). The rate coefficients at 300 K were suggested to be  $1.7 \times 10^{-9} \text{ cm}^3 \text{ s}^{-1}$  and  $7 \times 10^{-11} \text{ cm}^3 \text{ s}^{-1}$  for reactions (1)–(2) (Schilke et al. 1991), respectively. In the RATE12 chemical network, the same paths to form its isomer  $\text{H}_2\text{NC}^+$  exist with the rate coefficients of  $1.5 \times 10^{-9} \text{ cm}^3 \text{ s}^{-1}$  and  $6.7 \times 10^{-11} \text{ cm}^3 \text{ s}^{-1}$  at 10 K (Smith & Adams 1977; Fehsenfeld 1976). The rate coefficient of reaction (1) agrees with the latest calculations within uncertainties (Martinez et al. 2008). Hence, these values are comparable to the values of Schilke et al. (1991). This would be expected if the branching ratios of reactions to form  $\text{HCNH}^+$  and  $\text{H}_2\text{NC}^+$  are identical. Hence, we simply take the latter two values for reactions (1)–(2). Based on previous studies, the rate coefficient of reaction (7) is  $9 \times 10^{-10} \text{ cm}^3 \text{ s}^{-1}$  at 10 K (Knight et al. 1988; Loison et al. 2014b). These values are thus used for the qualitative calculations.

Based on our chemical modeling results and the rate coefficients discussed above, we can estimate the rates of reactions (1)–(7) to assess the relative importance of these formation paths as a function of time. Because reactions (1), (2), and (7) are not included in our modeling calculations, we only took the molecular abundances from the modeling results to estimate the formation rates. Figure 22 presents the comparison of the reaction rates for the chemical model using a number density of  $10^4 \text{ cm}^{-3}$ . We surprisingly find that reaction (7) involving the hydrogenation of  $\text{C}_2\text{N}^+$  emerges as the dominant formation pathway for  $\text{HCNH}^+$ , superseding all other competing reactions by several orders of magnitude. We investigate the modeling re-

sults with an updated chemical network augmented with reaction (7) in Appendix C, which suggests that reaction (7) can make significant contributions to the formation of  $\text{HCNH}^+$  at least on simulated timescales of  $< 10^5 \text{ yr}$ . This further casts doubts on the main formation path of  $\text{HCNH}^+$  via reactions (1)–(6). Furthermore, reaction (2) is as efficient as reactions (5)–(6) at timescales on the order of  $\lesssim 10^5 \text{ years}$ . On the other hand, reaction (1) is relatively less efficient, but becomes non-negligible at a timescale of  $\sim 10^6 \text{ years}$  when compared with reactions (2)–(6). The significance of missing reactions, particularly reaction (7), in the formation of  $\text{HCNH}^+$  is underscored by this comparison. More complete chemical networks and laboratory efforts to derive accurate rate coefficients will help to improve our understanding of the chemistry of  $\text{HCNH}^+$  and eventually larger nitrogen-bearing molecules.

#### 4.3. Collisional excitation

Owing to its small dipole moment (0.29 D; Botschwina 1986), the low  $J$  transitions of  $\text{HCNH}^+$  have Einstein A coefficients of  $< 5 \times 10^{-6} \text{ s}^{-1}$  (see Table 1), which are an order of magnitude lower than those of the other molecular transitions used in this work. By utilizing the latest rate coefficients governing collisions with  $\text{H}_2$ <sup>14</sup> (Bop, C., priv. comm) and Eq. (4) in Shirley (2015), we have calculated the optically thin critical densities of  $\text{HCNH}^+$  (1–0), (2–1), (3–2) at 10 K to be  $2.0 \times 10^2 \text{ cm}^{-2}$ ,  $1.7 \times 10^3 \text{ cm}^{-2}$ , and  $5.2 \times 10^3 \text{ cm}^{-2}$ , respectively. Intriguingly, these critical densities are even lower than the corresponding low- $J$  CO critical densities in the optically thin regime (Yang et al. 2010), implying that the energy levels connecting these  $\text{HCNH}^+$  transitions in LTE and can trace low-density regions. Therefore, we argue that  $\text{HCNH}^+$  can be regarded as a good probe of pristine molecular gas prior to the onset of gravitational collapse.

Recent studies have suggested that electrons may play a significant role in the excitation of molecular tracers like HCN and CH in molecular clouds (Goldsmith & Kauffmann 2017; Jacob et al. 2021). Adopting the same approximation that the collisional cross sections for electron excitation will be dominated by long-range forces and scale as the square of the permanent electric dipole moment (Goldsmith & Kauffmann 2017), we can derive the  $\text{HCNH}^+ - e^-$  collisional rates by scaling the values of the  $\text{HCN} - e^-$  and  $\text{CH}^+ - e^-$  collisional rates from Faure et al. (2007) and Faure et al. (2017). Because the dipole moment (0.29 D) of  $\text{HCNH}^+$  is about 0.10 and 0.17 times those of HCN (2.985 D; Ebenstein & Muentner 1984) and  $\text{CH}^+$  (1.683 D; Cheng et al. 2007), the  $\text{HCNH}^+ - e^-$  collisional rates are found to be  $\sim 2 \times 10^{-13} \text{ cm}^3 \text{ s}^{-1}$  and  $\sim 1 \times 10^{-12} \text{ cm}^3 \text{ s}^{-1}$ , respectively. Utilizing these values, we can estimate the critical electron fractional abundance that is required to make the electron collision rate equal to the  $\text{H}_2$  collision rate,  $x^*(e^-) = n_c(e^-)/n_c(\text{H}_2)$  (Goldsmith & Kauffmann 2017).  $x^*(e^-)$  is found to be  $\sim (1 - 4) \times 10^{-3}$ , which is considerably greater than the expected electron abundances of a few  $10^{-9}$  in molecular clouds (Caselli et al. 2002b). On the other hand, molecular clouds with  $\text{H}_2$  number densities of  $\gtrsim 5 \times 10^3 \text{ cm}^{-3}$  are sufficient to thermalize the excitation temperatures due to the low critical  $\text{H}_2$  densities of the three low  $J$   $\text{HCNH}^+$  transitions. Therefore, we conclude that electron collisions with  $\text{HCNH}^+$  are unlikely to be significant in molecular clouds. We also note that the approximation of  $x^*(e^-)$  is very

<sup>14</sup> The adopted collisional rate coefficients are more accurate than those presented in Bop & Lique (2023), because the  $j = 2$  excited energy level of  $\text{H}_2$  has been taken into account in the latest results (Bop, C., priv. comm).

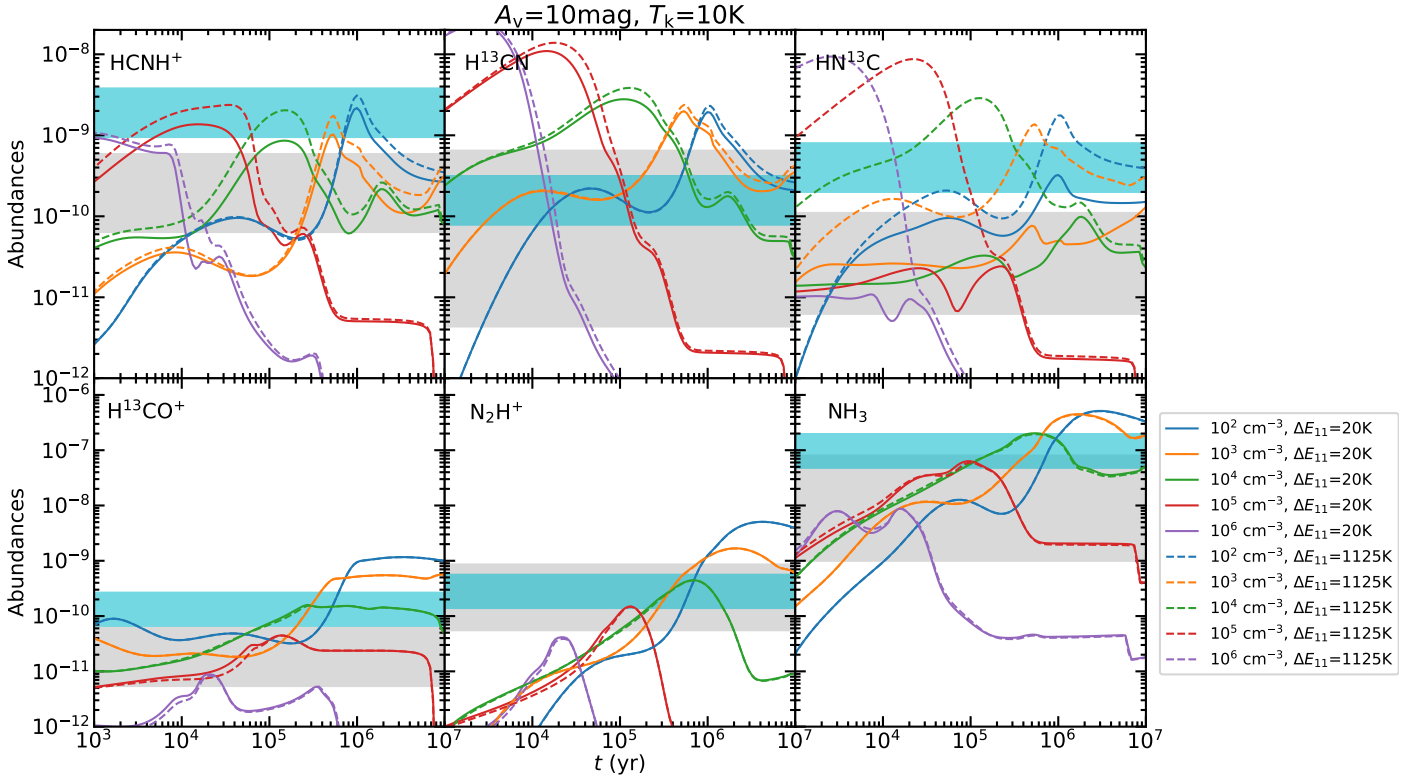


**Fig. 19.** Molecular abundances relative to  $\text{H}_2$  as a function of time, estimated from *Chempl* (Du 2021). The different colors correspond to the different  $\text{H}_2$  number densities from  $10^2 \text{ cm}^{-3}$  to  $10^6 \text{ cm}^{-3}$ . The solid and dashed lines represent the modeling results with the energy barrier  $\Delta E_{11} = 20 \text{ K}$  and  $\Delta E_{11} = 1125 \text{ K}$  for reaction (11), respectively. The observed molecular abundances in our studies are indicated by the grey shaded regions, while the molecular abundances in TMC1 (Agúndez & Wakelam 2013) are indicated by the cyan shaded regions.

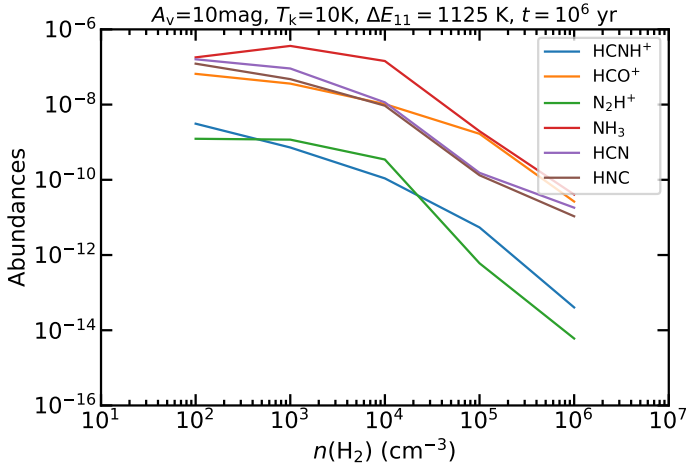


**Fig. 20.** Molecular abundances of  $\text{HCNH}^+$ ,  $\text{HCN}$ ,  $\text{HNC}$ ,  $\text{HCO}^+$ ,  $\text{N}_2\text{H}^+$ , and  $\text{NH}_3$  as a function of  $\text{H}_2$  number density at a simulated timescale of  $10^6 \text{ yr}$ . The adopted physical conditions are indicated on the top of this panel.

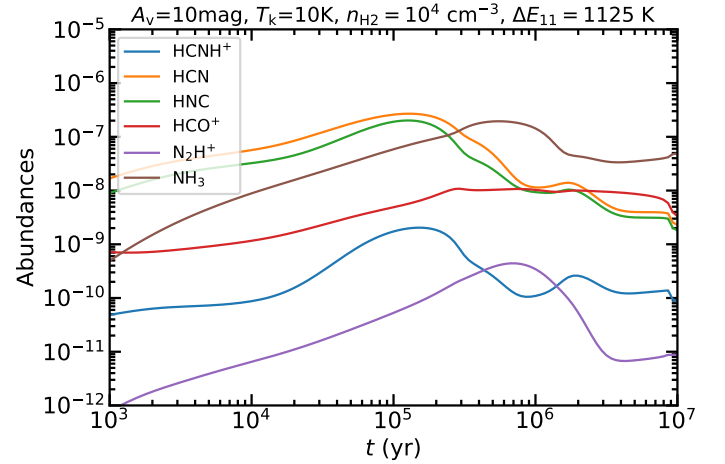


**Fig. 21.** Temporal evolution of the abundances of  $\text{HCNH}^+$ ,  $\text{HCN}$ ,  $\text{HNC}$ ,  $\text{HCO}^+$ ,  $\text{N}_2\text{H}^+$ , and  $\text{NH}_3$ , estimated from *Chempl* (Du 2021). The adopted physical conditions are indicated on the top of this panel.

crude especially in the case of ion-electron interactions, because the dipole moment is no longer the only dominant term in the long-range forces.

## 5. Summary and outlook

Using the IRAM-30 m and APEX-12 m telescopes, we have mapped  $\text{HCNH}^+$ ,  $\text{H}^{13}\text{CN}$ ,  $\text{HN}^{13}\text{C}$ ,  $\text{H}^{13}\text{CO}^+$ , and  $\text{N}_2\text{H}^+$  transi-

tions toward the Serpens filament and Serpens South. Our primary findings are summarized below:

1. Our observations of the two regions provide the first reliable distributions of  $\text{HCNH}^+$ , which suggests that  $\text{HCNH}^+$  is abundant in cold and quiescent regions but shows a deficit toward star-forming regions (i.e., emb10, the Serpens South cluster).

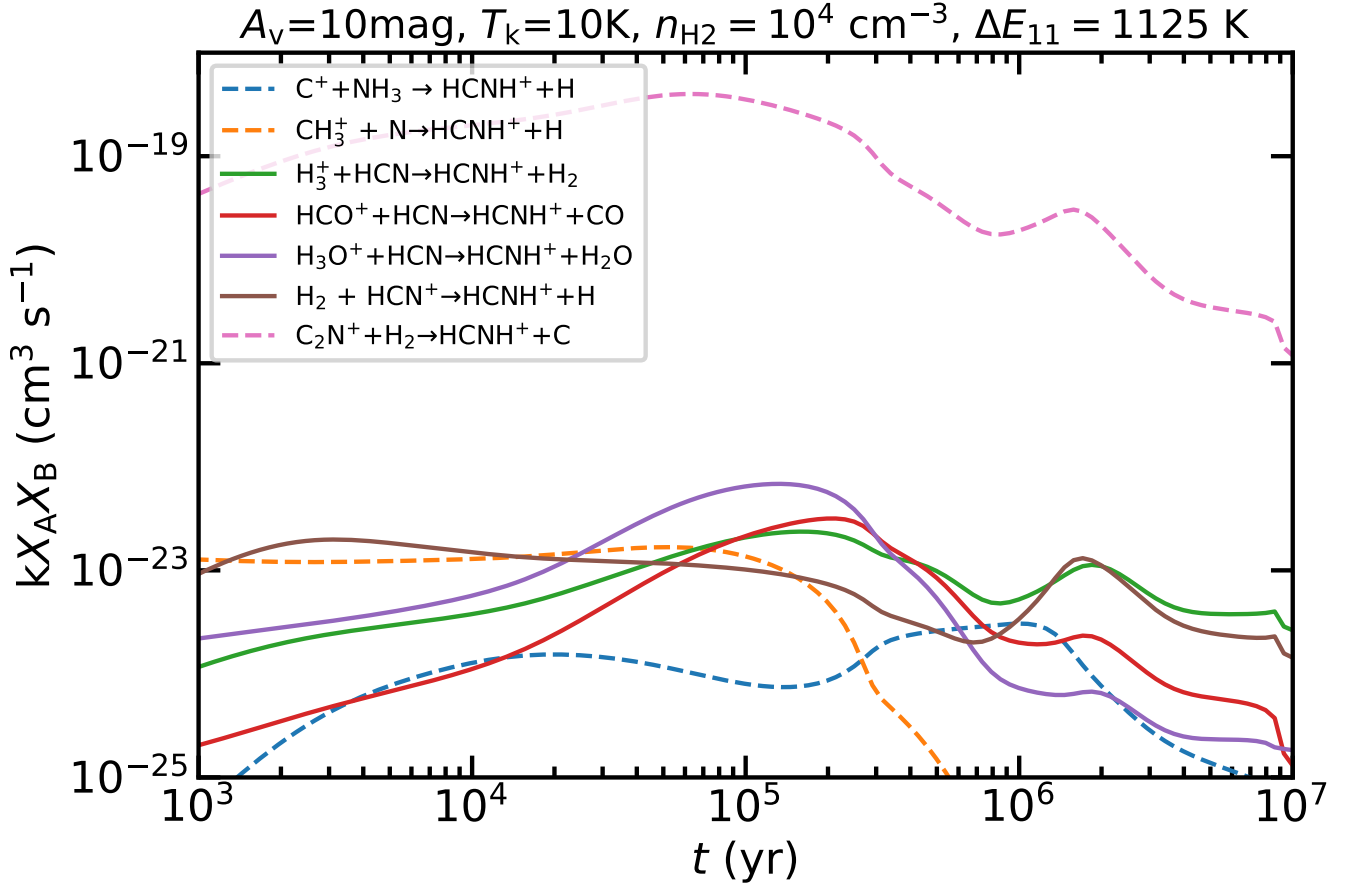


**Fig. 22.** Reaction rates of the different formation paths of  $\text{HCNH}^+$  as a function of time. The solid lines indicate reactions that are included in the RATE12 chemical network, whereas the dashed lines include potentially important reactions not incorporated in the network.

2. An LTE analysis suggests that the observed  $\text{HCNH}^+$  column densities range from  $4.2 \times 10^{12} \text{ cm}^{-2}$  to  $2.7 \times 10^{13} \text{ cm}^{-2}$ , which leads to its corresponding abundance relative to  $\text{H}_2$  ranging from  $3.1 \times 10^{-11}$  in protostellar cores to  $5.9 \times 10^{-10}$  in prestellar cores.  $\text{HCNH}^+$  is more abundant in molecular cores prior to gravitational collapse than in prestellar and star-forming cores. This result is in agreement with the scenario that  $\text{HCNH}^+$  abundances decrease as the region evolves.
3. Based on our observations, we find that  $\text{HCNH}^+$  abundances generally decrease with increasing  $\text{H}_2$  column density. We suggest that  $\text{HCNH}^+$  destruction in cold environments ( $T_g \sim 10 \text{ K}$ ) mainly depends on the increased  $\text{H}_2$  number density which causes the freeze-out of its precursors HCN and HNC.
4. Current astrochemical models cannot explain the observed trend in SSN1 where the  $\text{HCNH}^+$  abundance shows an anti-correlation with HCN and HNC, but shows a positive correlation with  $\text{N}_2\text{H}^+$  and  $\text{NH}_3$ . This indicates that additional formation paths of  $\text{HCNH}^+$  from molecules (e.g.,  $\text{N}_2$  and  $\text{NH}_3$ ) that do not freeze out should play an important role in the formation of  $\text{HCNH}^+$  in the freeze-out regions where HCN and HNC are heavily depleted.
5. Comparing the reaction rates of possible formation paths of  $\text{HCNH}^+$ , we find that important chemical reactions for

the formation of  $\text{HCNH}^+$  are likely missing in the RATE12 chemical network. More complete chemical networks and accurate rate coefficients are indispensable to understand the chemistry of  $\text{HCNH}^+$ .

6. The optically thin critical densities for  $\text{HCNH}^+$  (1–0), (2–1), (3–2) at 10 K, resulting from collisions with  $\text{H}_2$  molecules, are found to be  $2.0 \times 10^2 \text{ cm}^{-2}$ ,  $1.7 \times 10^3 \text{ cm}^{-2}$ , and  $5.2 \times 10^3 \text{ cm}^{-2}$ , respectively. These values suggest that LTE for these transitions should be readily achieved in molecular clouds. Since LTE is a good approximation for  $\text{HCNH}^+$ , the derived  $\text{HCNH}^+$  column densities should be reliable (see Table 3). On the other hand, electron excitation plays a negligible role for these transitions in molecular clouds.

Our observations have shown that  $\text{HCNH}^+$  appears to become deficient after the onset of gravitational collapse in low-mass star formation regions (see also Appendix B). However, the observational picture toward other environments is still elusive. Although  $\text{HCNH}^+$  has already been detected in a number of high-mass star formation regions (e.g., Fontani et al. 2021), the influence of the environment on its spatial distribution is not well investigated in such environments. We also searched for information on  $\text{HCNH}^+$  in previous line surveys of the circumstellar envelopes of evolved stars.  $\text{HCNH}^+$  (2–1) has been observed in the 2 mm line survey of the asymptotic giant branch star IRC+10216 (Cernicharo et al. 2000; He et al.

2008) and  $\text{HCNH}^+$  (3–2) has been covered in the 1 mm line survey of IRC+10216 and the red supergiant VY CMA (Tenenbaum et al. 2010; Kamiński et al. 2013), but the  $\text{HCNH}^+$  transitions were not detected by these sensitive surveys. This indicates that this molecular ion might not be abundant in circumstellar envelopes of evolved stars. For extra-galactic observations, this molecule appears to be tentatively detected in NGC 4945 (Villicana Pedraza et al. 2016; Villicana-Pedraza et al. 2017).

## ACKNOWLEDGMENTS

We acknowledge the IRAM-30 m and APEX-12 m staff for their assistance with our observations. Y.G. is grateful to Ashly Sebastine for her preliminary investigation of the APEX-12 m pointed observations toward Serpens South. Fujun Du is supported by the National Natural Science Foundation of China (NSFC) through grants 12041305 and 11873094. C. H. has been funded by Chinese Academy of Sciences President's International Fellowship Initiative under Grant No. 2022VMA0018. A.M.J. acknowledges support by USRA through a grant for SOFIA Program 08-0038. X.D.T. acknowledges the support of the Natural Science Foundation of Xinjiang Uygur Autonomous Region under Grant No. 2022D01E06, the Tianshan Talent Program of Xinjiang Uygur Autonomous Region under Grant No. 2022TSYCLJ0005, and the Chinese Academy of Sciences "Light of West China" Program under Grant No. xzbzgz-zdsys-202212. C. Bop acknowledges financial support from the European Research Council (Consolidator Grant COLLEXISM, Grant Agreement No. 811363). M.R.R. is a Jansky Fellow of the National Radio Astronomy Observatory, USA. The research leading to these results has received funding from the European Union's Horizon 2020 research and innovation program under grant agreement No 101004719 [Opticon RadioNet Pilot ORP]. This publication is based on data acquired with the Atacama Pathfinder Experiment (APEX). APEX is a collaboration between the Max-Planck-Institut für Radioastronomie, the European Southern Observatory, and the Onsala Space Observatory. This research has made use of NASA's Astrophysics Data System. This work also made use of Python libraries including Astropy<sup>15</sup> (Astropy Collaboration et al. 2013), NumPy<sup>16</sup> (van der Walt et al. 2011), SciPy<sup>17</sup> (Jones et al. 2001), Matplotlib<sup>18</sup> (Hunter 2007), APLpy (Robitaille & Bressert 2012), and seaborn<sup>19</sup> (Waskom 2021). We would like to thank the anonymous referee for helpful comments.

## References

- Aalto, S., Polatidis, A. G., Hüttemeister, S., & Curran, S. J. 2002, *A&A*, 381, 783
- Agúndez, M. & Wakelam, V. 2013, *Chemical Reviews*, 113, 8710
- André, P., Men'shchikov, A., Bontemps, S., et al. 2010, *A&A*, 518, L102
- Astropy Collaboration, Robitaille, T. P., Tollerud, E. J., et al. 2013, *A&A*, 558, A33
- Behrens, E., Mangum, J. G., Holdship, J., et al. 2022, *ApJ*, 939, 119
- Belloche, A. & André, P. 2004, *A&A*, 419, L35
- Belloche, A., Maury, A. J., Maret, S., et al. 2020, *A&A*, 635, A198
- Bergin, E. A., Alves, J., Huard, T., & Lada, C. J. 2002, *ApJ*, 570, L101
- Bergin, E. A. & Tafalla, M. 2007, *ARA&A*, 45, 339
- Bop, C. T. & Lique, F. 2023, *J. Chem. Phys.*, 158, 074304
- Botschwina, P. 1986, *Chemical Physics Letters*, 124, 382
- Burkhardt, A. M., Loomis, R. A., Shingledecker, C. N., et al. 2021, *Nature Astronomy*, 5, 181
- Carter, M., Lazareff, B., Maier, D., et al. 2012, *A&A*, 538, A89
- Caselli, P., Benson, P. J., Myers, P. C., & Tafalla, M. 2002a, *ApJ*, 572, 238
- Caselli, P., Walmsley, C. M., Tafalla, M., Dore, L., & Myers, P. C. 1999, *ApJ*, 523, L165
- Caselli, P., Walmsley, C. M., Zucconi, A., et al. 2002b, *ApJ*, 565, 344
- Cernicharo, J., Castets, A., Duvert, G., & Guilloteau, S. 1984, *A&A*, 139, L13
- Cernicharo, J., Guélin, M., & Kahane, C. 2000, *A&AS*, 142, 181
- Cheng, M., Brown, J. M., Rosmus, P., et al. 2007, *Phys. Rev. A*, 75, 012502
- Cravens, T. E., Robertson, I. P., Waite, J. H., et al. 2006, *Geophys. Res. Lett.*, 33, L07105
- Draine, B. T. 1978, *ApJS*, 36, 595
- Du, F. 2021, *Research in Astronomy and Astrophysics*, 21, 077
- Dzib, S., Loinard, L., Mioduszewski, A. J., et al. 2010, *ApJ*, 718, 610
- Ebenstein, W. L. & Muenter, J. S. 1984, *J. Chem. Phys.*, 80, 3989
- Endres, C. P., Schlemmer, S., Schilke, P., Stutzki, J., & Müller, H. S. P. 2016, *Journal of Molecular Spectroscopy*, 327, 95
- Enoch, M. L., Evans, Neal J., I., Sargent, A. I., & Glenn, J. 2009, *ApJ*, 692, 973
- Enoch, M. L., Glenn, J., Evans, II, N. J., et al. 2007, *ApJ*, 666, 982
- Faure, A., Halvick, P., Stoecklin, T., et al. 2017, *MNRAS*, 469, 612
- Faure, A., Varambhia, H. N., Stoecklin, T., & Tennyson, J. 2007, *MNRAS*, 382, 840
- Fehsenfeld, F. C. 1976, *ApJ*, 209, 638
- Fiorellino, E., Elia, D., André, P., et al. 2021, *MNRAS*, 500, 4257
- Fixsen, D. J. 2009, *ApJ*, 707, 916
- Fontani, F., Colzi, L., Redaelli, E., Sipilä, O., & Caselli, P. 2021, *A&A*, 651, A94
- Friesen, R. K., Bourke, T. L., Di Francesco, J., Gutermuth, R., & Myers, P. C. 2016, *ApJ*, 833, 204
- Friesen, R. K., Medeiros, L., Schnee, S., et al. 2013, *MNRAS*, 436, 1513
- Ginsburg, A. & Mirocha, J. 2011, *PySpecKit: Python Spectroscopic Toolkit*, *Astrophysics Source Code Library*, record ascl:1109.001
- Glenn, J., Ade, P. A. R., Amarie, M., et al. 2003, in *Society of Photo-Optical Instrumentation Engineers (SPIE) Conference Series*, Vol. 4855, *Millimeter and Submillimeter Detectors for Astronomy*, ed. T. G. Phillips & J. Zmuidzinas, 30–40
- Goicoechea, J. R., Lique, F., & Santa-Maria, M. G. 2022, *A&A*, 658, A28
- Goldsmith, P. F. & Kauffmann, J. 2017, *ApJ*, 841, 25
- Gong, Y., Belloche, A., Du, F. J., et al. 2021, *A&A*, 646, A170
- Gong, Y., Belloche, A., Du, F. J., et al. 2023, *A&A*, 672, C1
- Gong, Y., Li, G. X., Mao, R. Q., et al. 2018, *A&A*, 620, A62
- Graninger, D. M., Herbst, E., Öberg, K. I., & Vasyunin, A. I. 2014, *ApJ*, 787, 74
- Güsten, R., Nyman, L. Å., Schilke, P., et al. 2006, *A&A*, 454, L13
- Gutermuth, R. A., Bourke, T. L., Allen, L. E., et al. 2008, *ApJ*, 673, L151
- Hacar, A., Bosman, A. D., & van Dishoeck, E. F. 2020, *A&A*, 635, A4
- He, J. H., Dinh-V-Trung, Kwok, S., et al. 2008, *ApJS*, 177, 275
- Herbst, E. 1978, *ApJ*, 222, 508
- Herbst, E. & Klemperer, W. 1973, *ApJ*, 185, 505
- Herbst, E., Terzieva, R., & Talbi, D. 2000, *MNRAS*, 311, 869
- Hezareh, T., Houde, M., McCoe, C., Vastel, C., & Peng, R. 2008, *ApJ*, 684, 1221
- Hirota, T., Yamamoto, S., Mikami, H., & Ohishi, M. 1998, *ApJ*, 503, 717
- Hunter, J. D. 2007, *Computing in Science & Engineering*, 9, 90
- Jacob, A. M., Menten, K. M., Wiesemeyer, H., & Ortiz-León, G. N. 2021, *A&A*, 650, A133
- Jin, M., Lee, J.-E., & Kim, K.-T. 2015, *ApJS*, 219, 2
- Jones, E., Oliphant, T., Peterson, P., et al. 2001, *SciPy: Open source scientific tools for Python*
- Jørgensen, J. K., Belloche, A., & Garrod, R. T. 2020, *ARA&A*, 58, 727
- Kamiński, T., Gottlieb, C. A., Menten, K. M., et al. 2013, *A&A*, 551, A113
- Kirk, H., Myers, P. C., Bourke, T. L., et al. 2013, *ApJ*, 766, 115
- Klein, B., Hochgürtel, S., Krämer, I., et al. 2012, *A&A*, 542, L3
- Knight, J. S., Petrie, S. A. H., Freeman, C. G., et al. 1988, *Journal of the American Chemical Society*, 110, 5286, PMID: 11538327
- Könyves, V., André, P., Men'shchikov, A., et al. 2015, *A&A*, 584, A91
- Lefloch, B., Bachiller, R., Ceccarelli, C., et al. 2018, *MNRAS*, 477, 4792
- Levshakov, S. A., Henkel, C., Reimers, D., & Wang, M. 2014, *A&A*, 567, A78
- Levshakov, S. A., Henkel, C., Reimers, D., et al. 2013, *A&A*, 553, A58
- Li, J., Shen, Z.-Q., Wang, J., et al. 2016, *ApJ*, 824, 136
- Loison, J.-C., Wakelam, V., & Hickson, K. M. 2014a, *MNRAS*, 443, 398
- Loison, J.-C., Wakelam, V., Hickson, K. M., Bergeat, A., & Mereau, R. 2014b, *MNRAS*, 437, 930
- Loughnane, R. M., Redman, M. P., Thompson, M. A., et al. 2012, *MNRAS*, 420, 1367
- Mangum, J. G. & Shirley, Y. L. 2016, *Corrigendum: How to Calculate Molecular Column Density*, *Publications of the Astronomical Society of the Pacific*, Volume 128, Issue 960, pp. 029201 (2016).
- Martinez, Oscar, J., Betts, N. B., Villano, S. M., et al. 2008, *ApJ*, 686, 1486

Maury, A. J., André, P., Men'shchikov, A., Könyves, V., & Bontemps, S. 2011, *A&A*, 535, A77

McElroy, D., Walsh, C., Markwick, A. J., et al. 2013, *A&A*, 550, A36

Mendes, M. B., Buhr, H., Berg, M. H., et al. 2012, *ApJ*, 746, L8

Mottram, J. C., van Dishoeck, E. F., Kristensen, L. E., et al. 2017, *A&A*, 600, A99

Mouschovias, T. C. & Ciolek, G. E. 1999, in *NATO Advanced Study Institute (ASI) Series C, Vol. 540, The Origin of Stars and Planetary Systems*, ed. C. J. Lada & N. D. Kylafis, 305

Muders, D., Hafok, H., Wyrowski, F., et al. 2006, *A&A*, 454, L25

Nakamura, F., Sugitani, K., Shimajiri, Y., et al. 2011, *ApJ*, 737, 56

Nakamura, F., Sugitani, K., Tanaka, T., et al. 2014, *ApJ*, 791, L23

Ortiz-León, G. N., Dzib, S. A., Kounkel, M. A., et al. 2017, *ApJ*, 834, 143

Ortiz-León, G. N., Dzib, S. A., Loinard, L., et al. 2023, *A&A*, 673, L1

Ortiz-León, G. N., Loinard, L., Dzib, S. A., et al. 2018, *ApJ*, 869, L33

Ortiz-León, G. N., Plunkett, A. L., Loinard, L., et al. 2021, *AJ*, 162, 68

Pacheco-Vázquez, S., Fuente, A., Agúndez, M., et al. 2015, *A&A*, 578, A81

Pety, J. 2005, in *SF2A-2005: Semaine de l'Astrophysique Française*, ed. F. Casoli, T. Contini, J. M. Hameury, & L. Pagani, 721

Plunkett, A. L., Arce, H. G., Corder, S. A., et al. 2015a, *ApJ*, 803, 22

Plunkett, A. L., Arce, H. G., Mardones, D., et al. 2015b, *Nature*, 527, 70

Pratap, P., Dickens, J. E., Snell, R. L., et al. 1997, *ApJ*, 486, 862

Quénard, D., Vastel, C., Ceccarelli, C., et al. 2017, *MNRAS*, 470, 3194

Robitaille, T. & Bressert, E. 2012, *APLpy: Astronomical Plotting Library in Python*

Schilke, P., Walmsley, C. M., Millar, T. J., & Henkel, C. 1991, *A&A*, 247, 487

Schilke, P., Walmsley, C. M., Pineau Des Forets, G., et al. 1992, *A&A*, 256, 595

Shiba, Y., Hirano, T., Nagashima, U., & Ishii, K. 1998, *J. Chem. Phys.*, 108, 698

Shirley, Y. L. 2015, *PASP*, 127, 299

Smith, D. & Adams, N. G. 1977, *Chemical Physics Letters*, 47, 145

Sun, J., Gutermuth, R. A., Wang, H., et al. 2022, *MNRAS*, 516, 5244

Takano, S., Nakai, N., & Kawaguchi, K. 2002, *PASJ*, 54, 195

Talbi, D., Ellinger, Y., & Herbst, E. 1996, *A&A*, 314, 688

Tanaka, T., Nakamura, F., Awazu, Y., et al. 2013, *ApJ*, 778, 34

Tenenbaum, E. D., Dodd, J. L., Milam, S. N., Woolf, N. J., & Ziurys, L. M. 2010, *ApJS*, 190, 348

Toelle, F., Ungerechts, H., Walmsley, C. M., Winnewisser, G., & Churchwell, E. 1981, *A&A*, 95, 143

Tritsis, A., Basu, S., & Federrath, C. 2023, *MNRAS*, 521, 5087

Turner, B. E., Amano, T., & Feldman, P. A. 1990, *ApJ*, 349, 376

Ulich, B. L. & Haas, R. W. 1976, *ApJS*, 30, 247

van der Tak, F. F. S. & van Dishoeck, E. F. 2000, *A&A*, 358, L79

van der Walt, S., Colbert, S. C., & Varoquaux, G. 2011, *Computing in Science Engineering*, 13, 22

Villicana-Pedraza, I., Martín, S., Martín-Pintado, J., et al. 2017, in *Formation and Evolution of Galaxy Outskirts*, ed. A. Gil de Paz, J. H. Knapen, & J. C. Lee, Vol. 321, 305–305

Villicana Pedraza, I., Guesten, R., Armijos Abendaño, J., et al. 2016, in 41st COSPAR Scientific Assembly, Vol. 41, F3.1–27–16

Walmsley, C. M., Churchwell, E., Nash, A., & Fitzpatrick, E. 1982, *ApJ*, 258, L75

Waskom, M. L. 2021, *Journal of Open Source Software*, 6, 3021

Wilson, T. L. & Rood, R. 1994, *ARA&A*, 32, 191

Yan, Y. T., Henkel, C., Kobayashi, C., et al. 2023, *A&A*, 670, A98

Yang, B., Stancil, P. C., Balakrishnan, N., & Forrey, R. C. 2010, *ApJ*, 718, 1062

Zhang, M., Fang, M., Wang, H., et al. 2015, *ApJS*, 219, 21

Ziurys, L. M., Apponi, A. J., & Yoder, J. T. 1992, *ApJ*, 397, L123

Ziurys, L. M., Savage, C., Brewster, M. A., et al. 1999, *ApJ*, 527, L67

Ziurys, L. M. & Turner, B. E. 1986, *ApJ*, 302, L31

Zucker, C., Speagle, J. S., Schlafly, E. F., et al. 2019, *ApJ*, 879, 125

## Appendix A: Molecular column density maps

We present the column density maps of  $\text{H}^{13}\text{CN}$ ,  $\text{HN}^{13}\text{C}$ ,  $\text{H}^{13}\text{CO}^+$ , and  $\text{HCNH}^+$  in Figs. A.1–A.2.

## Appendix B: $\text{HCNH}^+$ in different evolutionary stages of low-mass star formation

Figure B.1 shows the  $\text{HCNH}^+$  spectra of low-mass star-formation regions in different environments. The  $\text{HCNH}^+$  spectra of TMC1, L1527, IRAS4A, L1157-mm, L1157-B1, SVS 13A, and L1448-R2 are based on IRAM-30 m observations, and the data are directly taken from the Large Program

‘Astrochemical Surveys At IRAM’ (ASAI<sup>20</sup>, Lefloch et al. 2018). This figure reveals that  $\text{HCNH}^+$  is only abundant in the early phases of low-mass star formation. During the Class 0 phase, L1527 is the only Class 0 object showing  $\text{HCNH}^+$  emission. This trend is consistent with our finding that the  $\text{HCNH}^+$  abundance decreases from the starless phase to the protostellar phase (see Fig. 12).

$\text{HCNH}^+$  is not detected in either the Class I object, SVS13A, or the shocked regions, L1157-B1 and L1148-R2. We also note that  $\text{HCNH}^+$  was not detected in the line survey toward the protoplanetary disc, AB Aur (Pacheco-Vázquez et al. 2015). This indicates that  $\text{HCNH}^+$  is not prominent in late stages of low-mass star formation.

## Appendix C: Updated chemical models

As demonstrated in Sect. 4.2, reaction (7) appears to play an important role in the formation of  $\text{HCNH}^+$ . Consequently, we have embarked on an exploration of chemical models, augmenting the existing chemical network with the inclusion of reaction (7). The results of this endeavor are displayed in Fig. C.1, which showcases modeling results under fixed physical conditions with  $A_V=10$  mag,  $T_g=10$  K, and  $n_{\text{H}_2} = 10^4 \text{ cm}^{-3}$ . Compared to the results with the chemical network without reaction (7), we find that  $\text{HCNH}^+$ ,  $\text{H}^{13}\text{CN}$ , and  $\text{HN}^{13}\text{C}$  can reach higher abundances in the updated chemical models. Especially for a simulated timescale of  $\lesssim 10^5$  yr,  $\text{HCNH}^+$  abundances are much higher in the updated chemical models. The most substantial discrepancy emerges around  $10^4$  yr, exhibiting a factor of  $\sim 5$  difference.

We also revisit the formation rates with the updated chemical networks as in Fig. 22. The updated results are shown in Fig. C.2. Compared to Fig. 22, the formation rate of reaction (7) in the updated chemical model is significantly reduced by about four orders of magnitude. This is because reaction (7) cause the rapid decrease of the  $\text{C}_2\text{N}^+$  abundance in early time and the  $\text{C}_2\text{N}^+$  abundance is about four orders of magnitude lower than in Fig. 22. It is still worth noting that the formation rate of reaction (7) is still high before  $10^5$  yr when the freezeout process becomes more important. These facts demonstrate that reaction (7) can make significant contributions to the formation of  $\text{HCNH}^+$  at least at a simulated timescale of  $< 10^5$  yr.

On the other hand, our findings regarding the overall abundance evolution remain remarkably consistent beyond  $10^5$  yr in Fig. C.1, because the freeze-out process becomes dominant in driving the abundance evolution. Because our targets are expected to have ages of  $\gtrsim 10^5$  yr, the consistency between the models further strengthens the reliability of the results outlined in Sect. 4.2. The abundances of  $\text{H}^{13}\text{CO}^+$ ,  $\text{N}_2\text{H}^+$ , and  $\text{NH}_3$  are identical across the simulated timescales from both sets of modeling results, implying that reaction (7) plays a negligible role in determining the abundances of these particular species.

<sup>20</sup> <https://www.iram.fr/ILPA/LP007/>

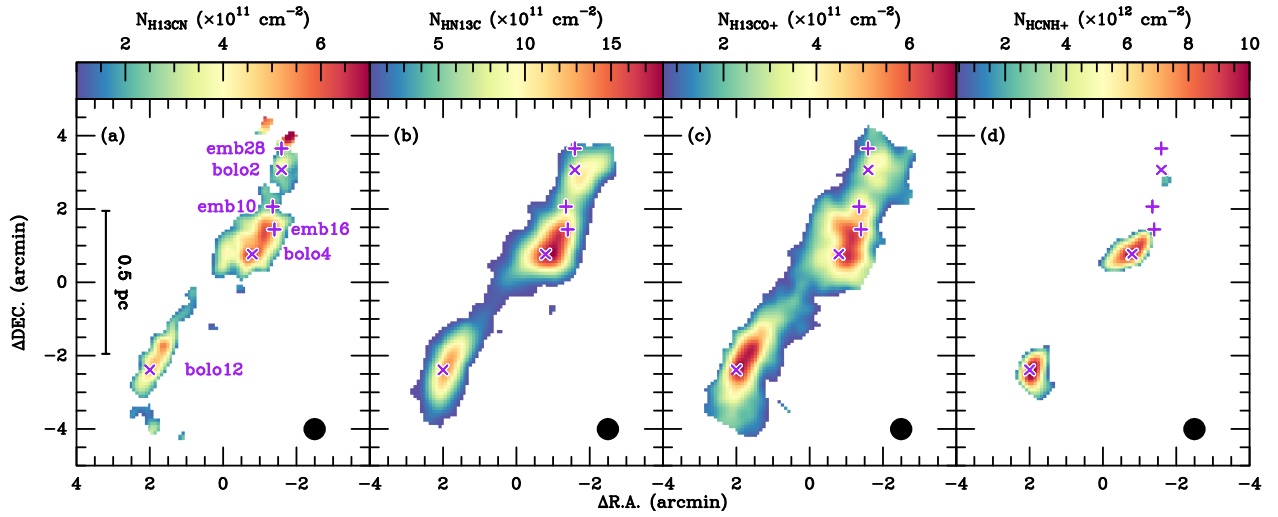


Fig. A.1. Molecular column density maps of the Serpens filament. The markers are the same as in Fig. 1.

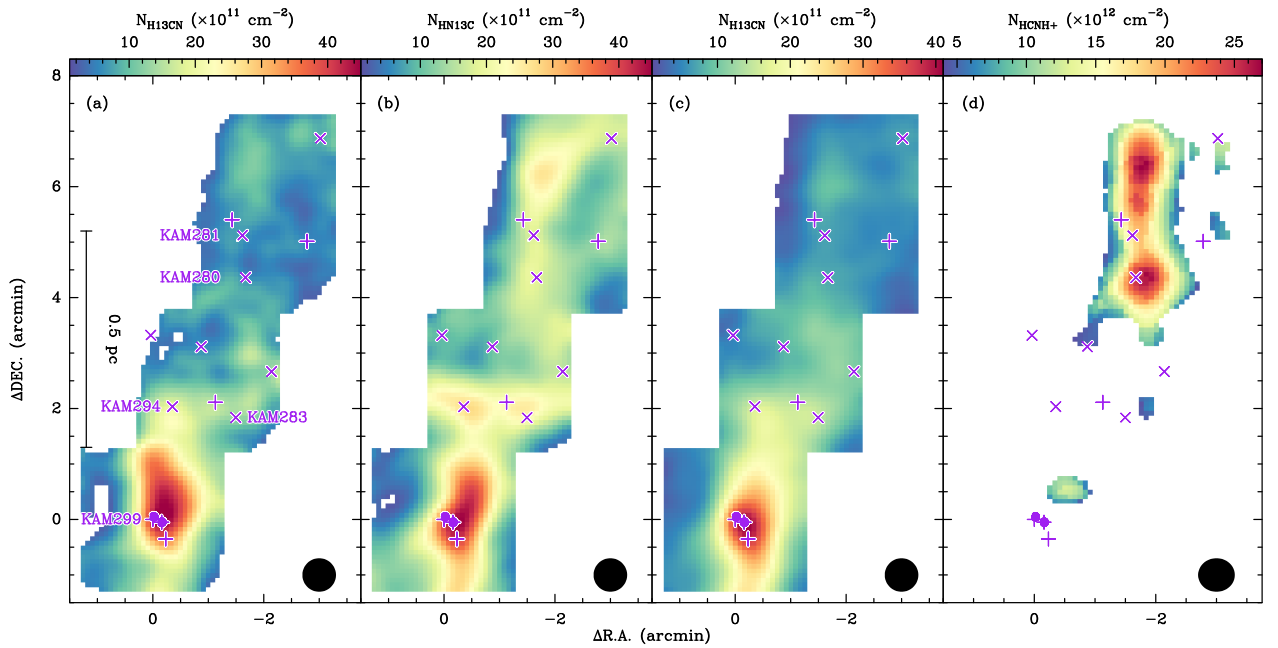
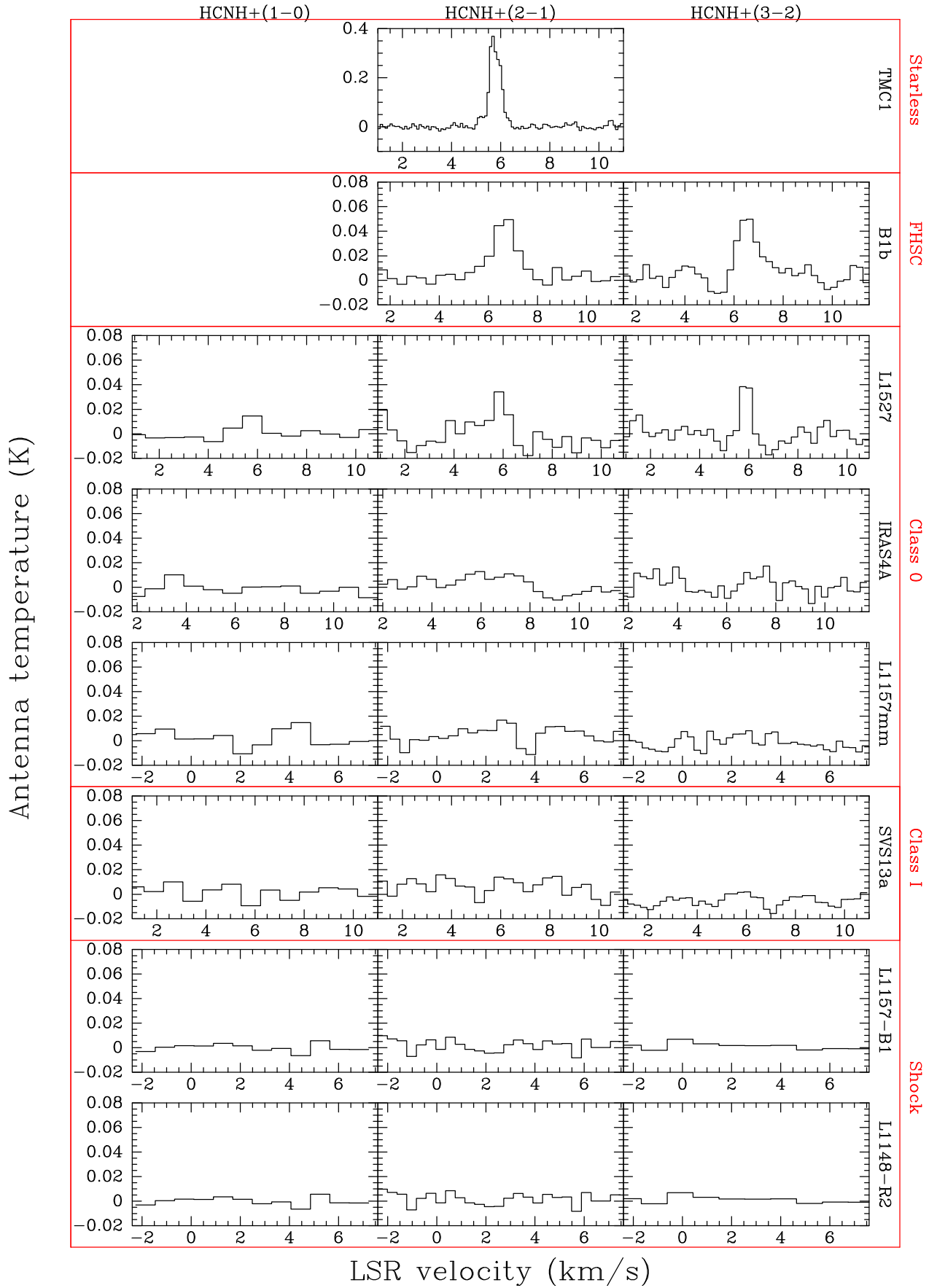
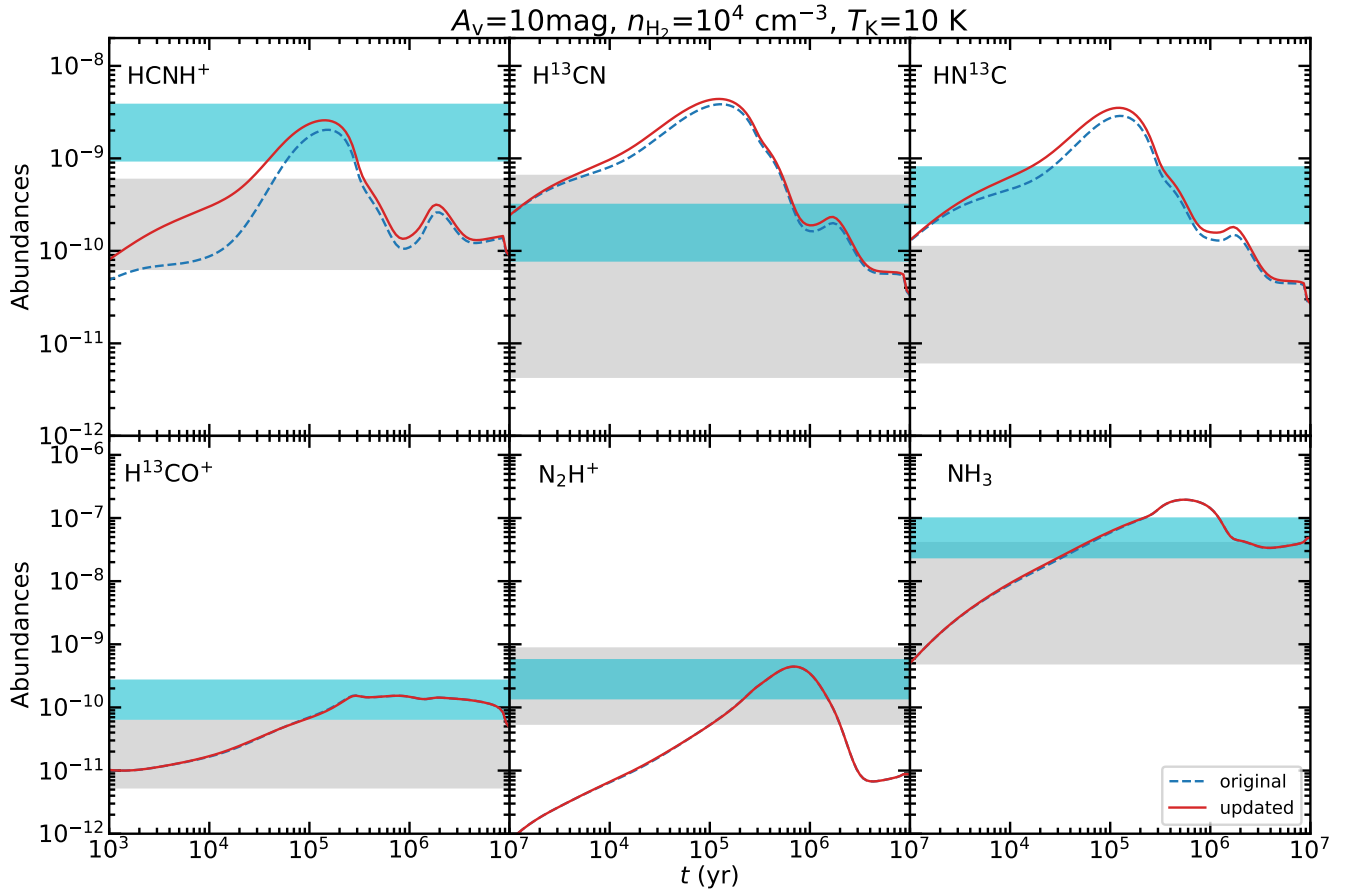


Fig. A.2. Molecular column density maps of Serpens South. The markers are the same as in Fig. 2.



**Fig. B.1.** ASAI  $\text{HCNH}^+$  spectra of TMC1, B1b, L1527, NGC1333-IRAS4A, L1157mm, NGC1333-SVS13a, L1157-B1, and L1148-R2 which represent different evolutionary stages, including starless cores, first hydrostatic cores (FHSCs), Class 0 protostars, Class I protostars, and shocked regions.  $\text{HCNH}^+$  (1-0), (2-1), and (3-2) are shown in the first, second, and third columns. The source name is indicated on the right side.



**Fig. C.1.** Molecular abundances relative to  $\text{H}_2$  as a function of time, calculated from *Chempl* (Du 2021). The dashed blue lines represent the modeling results in Sect. 4.2, while the solid red curves represent the modeling results obtained when including the reaction (7) to the underlying chemical network. The observed molecular abundances in our studies are indicated by the grey shaded regions, while the molecular abundances in TMC1 (Agúndez & Wakelam 2013) are indicated by the cyan shaded regions. The other physical conditions are indicated on the top of this figure.



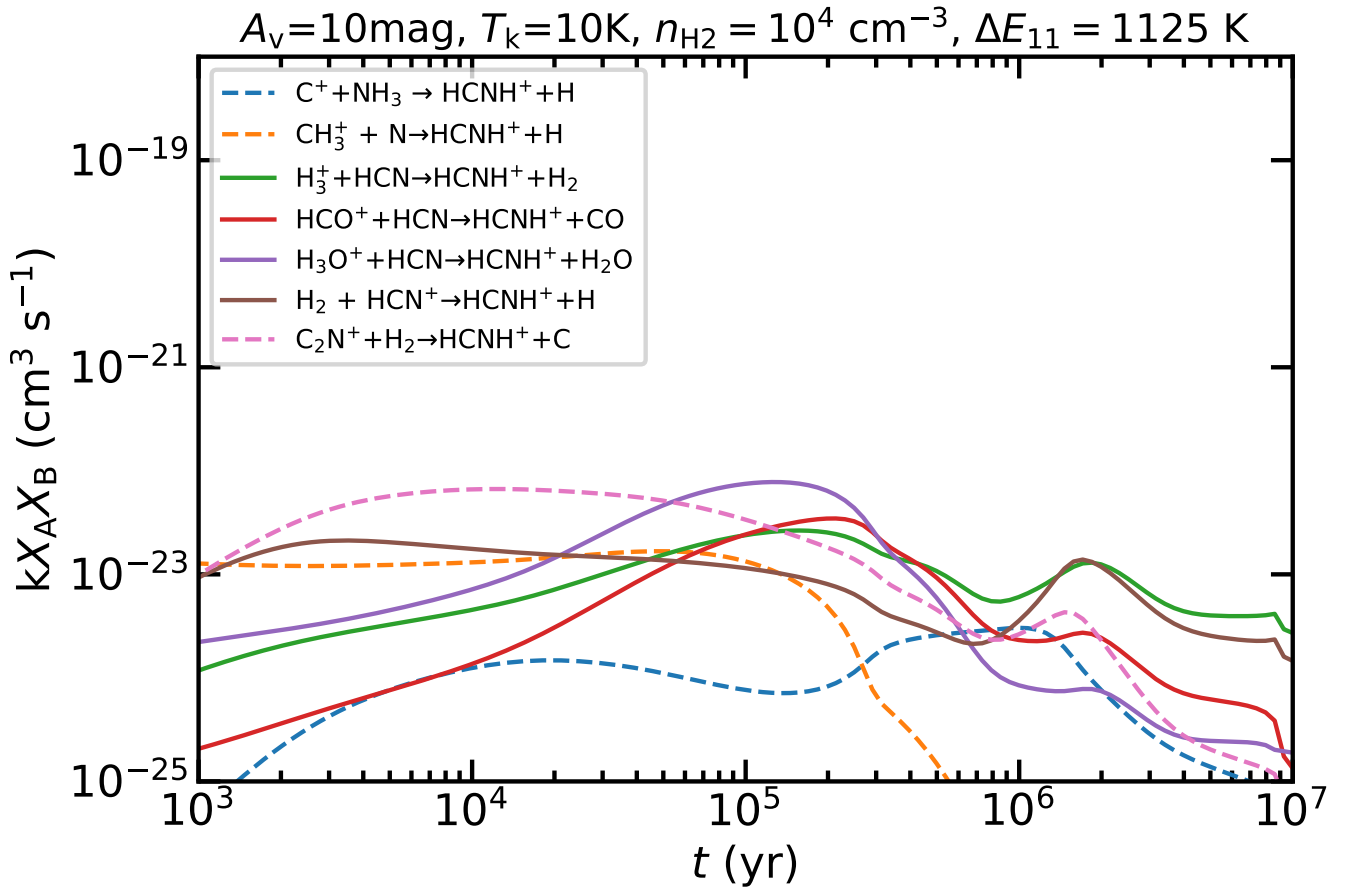


Fig. C.2. Same as Fig. 22 but for including the reaction (7) to the underlying chemical network.